Assessing the Performance of an Ocean Observing, Analysis and Forecast System for the Mid-Atlantic Bight Using Array Modes

by

Andrew M. Moore[1*], Julia Levin[2], Hernan G. Arango[2] and John Wilkin[2]

1: Department of Ocean Sciences, 1156 High Street, University of California, Santa Cruz CA 95062.
2: Department of Marine and Coastal Sciences, 71 Dudley Road, Rutgers University, New Brunswick NJ 08901.

* Corresponding author: ammoore@ucsc.edu

Abstract

The efficacy of an ocean observing, analysis, and forecasting system for the Mid-Atlantic Bight and the Gulf of Maine is explored using the concept of array modes. The analysis-forecast system is based on a triply nested configuration of the Regional Ocean Modeling System (ROMS) in conjunction with 4-dimensional variational (4D-Var) data assimilation. The array modes identify the degrees of freedom (*df*) of the signal and of the noise resolved by the observations, and are used here to quantify the extent to which the existing network of platforms and instruments are able to observe the ocean across different dynamical regimes ranging from quasi-geostrophic through the mesoscale and down to the sub-mesoscale. The ocean observing system includes the U.S. National Science Foundation's Ocean Observatories Initiative Pioneer Array. In general, it is found that the *df* of the signal are largely associated with *in situ* observations from the Pioneer Array. On the other hand, a combination of satellite remote sensing and *in situ* observations potentially contribute to the *df* of the noise associated with uncertainties in the measurements. The array modes also provide information about the reduction in the expected analysis and forecast error covariance due to assimilating the observations. Here too observations from the Pioneer Array are found to significantly influence the veracity of the analyses and forecasts, and the circulation is instrumental in propagating observational information to other parts of the model domain. An approach is presented in which the array modes are used to quantify the impact of data assimilation on the expected forecast error covariance of forecasts initialized from the 4D-Var ocean state estimates. The advantage of this approach over others in common use is that it is independent of forecast error norm and circumvents the need for generating potentially large and costly ensembles.

Keywords: Array modes; data assimilation; 4D-Var; Mid-Atlantic Bight; Pioneer Array; forecast error covariance

1 Introduction

Regional ocean analysis and forecasting are now well-established activities of many national agencies, operational centers, and research groups worldwide. A critical component of such systems is data assimilation, which aims to combine ocean observations with a model to yield an estimate of the ocean state that is more reliable than either the observations or model alone. Since the practice of data assimilation is deeply rooted in estimation theory, it also provides an opportunity to assess the properties of the observing system itself. In this study, we explore the array modes of the ocean observing system in the Mid-Atlantic Bight (MAB) and Gulf of Maine (GoM) in the NE Atlantic. This observing system supports the U.S. Integrated Ocean Observing System (IOOS) and forms the backbone of the Mid-Atlantic Regional Association Coastal Ocean Observing System (MARACOOS). The MAB is also unique in that it is home to the U.S. National Science Foundation (NSF) Ocean Observatories Initiative (OOI) Pioneer Array. The Pioneer Array has been operational since April 2014 and comprises fixed moorings and a fleet of autonomous underwater vehicles that are deployed at the continental shelf-break. The primary aim of the Pioneer Array is to increase understanding of the processes responsible for the transport of water masses across the shelf-break, and their relationship to atmospheric forcing on a range of time scales (Gawarkiewicz *et al.*, 2018).

This paper is an extension of the recent studies by Levin *et al.* (2019, 2020, 2021), which document a detailed assessment of the impact of the MAB and GoM observing system on data assimilation estimates of the ocean environment and shelf-break exchange processes in the vicinity of the Pioneer Array. Here, the array modes of the observing system have been used to delve deeper into the degree to which the information provided by the observations constrain our knowledge of the ocean state. The array modes are analogous to the characteristic modes employed in electrical engineering and antenna design. Array modes were first introduced in oceanography by Bennett (1985) and provide information about the field-of-view and degrees of freedom (*df*) of an observing system, as well as limitations that are endemic to the data assimilation system. More recent applications of array modes in ocean data assimilation include Egbert *et al.* (1994), Bennett (2002), Kurapov *et al.* (2009), and Kurapov and Özkan-Haller (2013), while modified forms of the array mode concept have been employed by Le Hénaff *et al.* (2009), Lamouroux *et al.* (2016) and Moore *et al.* (2018).

This study draws on the properties of, and information provided by, the array modes as a means of quantifying the efficacy of an ocean analysis-forecast system. Given their central importance, the concept of array modes is reviewed in section 2 in relation to 4-dimensional variational (4D-Var) data assimilation, the approach employed in this work. The concept of Reduced-rank Array Modes (RAMs) is a practical variant of the array mode concept and is also introduced in section 2. The model used in this study is the Regional Ocean Modeling System (ROMS) configured for the MAB and GoM in conjunction with 4D-Var as described in section 3. The model comprises a triply nested configuration of ROMS that resolves circulation scales ranging from quasi-geostrophic down to the sub-mesoscale. The 4D-Var analyses at each scale are informed by observations that lead to a reduction in the expected error covariance of the resulting ocean state estimates. As we will demonstrate, the reduction in error covariance can be quantified by drawing on the known properties of the RAMs. As a prelude, the hallmark fingerprints of the RAMs of the MAB and GoM ocean state estimates across the range of scales captured by the model are first explored in section 4. Section 5 focusses on several aspects of impact of the observations assimilated into the model on the 4D-Var analyses and ensuing ocean forecasts. First, section 5.1 describes an alternative and cost-effective RAM-based approach for computing the expected reduction in the analysis and forecast error covariance. The spatio-temporal nature of the expected error variance reduction in explored in section 5.2. In section 5.3 we demonstrate that much of the expected reduction in error covariance is associated with a single RAM. Furthermore, the contribution of each observation to the amplitude of this RAM is shown to be a useful and alternative measure of the observation impacts. The advantage of this approach over the more conventional adjoint-based (*e.g.* Langland and Baker, 2004) or ensemble-based approaches (*e.g.* Liu and Kalnay, 2008) is that it is independent of forecast error norm, and generally more cost-effective. Many of the ideas and results presented here are predicated on identification of the RAMs as the *dfs* of the observing system. This information is utilized in section 6 to identify the extent to which the 4D-Var analyses may be overly constrained by errors and uncertainties in the observations. A summary, conclusions, and discussion of potential applications of our work is presented in section 7.

2 Array Modes

The theory of array modes will be summarized here in terms of 4-dimensional variational (4D-Var) data assimilation, although, in principle, the same ideas can be applied to other linear data assimilation methodologies. With this in mind, we will follow standard notation and denote by $\boldsymbol{x}$ the ocean state-vector comprising all grid-point values of the model prognostic variables. Given a *prior* or background estimate of the state-vector, $\boldsymbol{x}^b$, and the $N \times 1$ vector of ocean observations, $\boldsymbol{y}^o$, where N is the number of observations, the best linear unbiased estimate or analysis, $\boldsymbol{x}^a$, is given by:

$$\boldsymbol{x}^a = \boldsymbol{x}^b + \boldsymbol{K}\left(\boldsymbol{y}^o - H(\boldsymbol{x}^b)\right) \qquad (1)$$

where H is the observation operator that samples $\boldsymbol{x}^b$ at the observation locations in space and time, and $\boldsymbol{K}$ is the gain matrix. In 4D-Var, H includes the nonlinear model. The gain can be expressed as:

$$\boldsymbol{K} = \boldsymbol{B}\boldsymbol{H}^T(\boldsymbol{H}\boldsymbol{B}\boldsymbol{H}^T + \boldsymbol{R})^{-1} \qquad (2)$$

where $\boldsymbol{B}$ and $\boldsymbol{R}$ are the background error and observation error covariance matrices, respectively. The matrix $\boldsymbol{H}$ denotes the tangent linearization of H and in 4D-Var represents the tangent linear model sampled at the observation points, while $\boldsymbol{H}^T$ denotes the adjoint of these operations.

The matrix $\boldsymbol{P} = (\boldsymbol{H}\boldsymbol{B}\boldsymbol{H}^T + \boldsymbol{R})$ represents the total error covariance in the space spanned by the observations and is often referred to as the stabilized representer matrix. For now, let us suppose that all of the observations are of the same type (*e.g.*, *in situ* temperature observations). In this case, and since $\boldsymbol{P}$ is a symmetric matrix, it can be factorized as $\boldsymbol{W}\boldsymbol{\Lambda}\boldsymbol{W}^T$ where $\boldsymbol{W} = (\boldsymbol{w}_i)$ is the matrix of orthonormal eigenvectors $\boldsymbol{w}_i$ and $\boldsymbol{\Lambda} = \mathrm{diag}(\lambda_i)$ are the associated eigenvalues. Following Bennett (1985), the analysis $\boldsymbol{x}^a$ in (1) can be re-expressed as:

$$\boldsymbol{x}^a = \boldsymbol{x}^b + \sum_{i=1}^{N} \alpha_i \boldsymbol{\Psi}_i \qquad (3)$$

where $\boldsymbol{\Psi}_i = \boldsymbol{B}\boldsymbol{H}^T\boldsymbol{w}_i$ are referred to as the array modes with amplitudes $\alpha_i = \lambda_i^{-1}\boldsymbol{w}_i^T\boldsymbol{d}$, and $\boldsymbol{d} = \left(\boldsymbol{y}^o - H(\boldsymbol{x}^b)\right)$ is the innovation vector. Similar ideas are utilized in antenna theory where it is the eigen spectrum of the impedance matrix associated with an antenna that is considered (Chen and Wang, 2015). In that case, the array modes (or *characteristic modes*) are frequency-dependent. The extent to which a particular mode is excited by an incident electromagnetic field with frequency ω is proportional to $(\lambda_i - \omega)^{-1}$. Therefore, when the incident waveform frequency matches the eigenvalue of a specific array mode, resonance occurs. The array modes of an ocean observing system depend on $\boldsymbol{B}$, $\boldsymbol{R}$, H, and, in the case of 4D-Var, $\boldsymbol{x}^b$ and, while dependent on the observation times and *locations* through H, they are independent of the observation values $\boldsymbol{y}^o$. However, the extent to which each array mode is *excited* is determined by the innovations $\boldsymbol{d}$ and therefore *does* depend on the data values themselves. In this case, there is no frequency dependence of the "incident signal" from the innovations, and the array mode amplitudes α_i are proportional to λ_i^{-1}.

The eigenvectors $\boldsymbol{w}_i$ represent the Empirical Orthogonal Functions (EOFs) of the total error covariance *in observation space*, and the eigenvalues are the variance associated with each EOF. Since the array mode amplitudes $\alpha_i \propto \lambda_i^{-1}$, the EOFs associated with the largest uncertainty are weighted the least, while the EOFs that account for the least fraction of error variance are weighted the most. This, of course, makes intuitive sense since the 4D-Var increments $\delta\boldsymbol{x} = \sum_{i=1}^{N} \alpha_i \boldsymbol{\Psi}_i$ then draw most heavily on the array modes associated with the smallest total error variance. The array modes themselves $\boldsymbol{\Psi}_i = \boldsymbol{B}\boldsymbol{H}^T\boldsymbol{w}_i$ represent the projection of the stabilized representer matrix EOFs $\boldsymbol{w}_i$ into state-space via the adjoint operation $\boldsymbol{H}^T$.

In general, ocean observing systems comprise observations of several state variables from a variety of different platforms. Also, since the number of observations N is large, most 4D-Var approaches identify the analysis given by (1) and (2) using iterative methods. Therefore, some form of preconditioning of $\boldsymbol{P}$ is essential, and without this, the notion of EOFs does not make sense. In ROMS, the $\boldsymbol{R}$-preconditioned stabilized representer matrix $\widetilde{\boldsymbol{P}} = (\boldsymbol{R}^{-1}\boldsymbol{H}\boldsymbol{B}\boldsymbol{H}^T + \boldsymbol{I})$ is factorized using the Lanczos formulation of the conjugate gradient (CG) algorithm according to:

$$\widetilde{\boldsymbol{P}}_m \approx \boldsymbol{V}_m\boldsymbol{T}_m\boldsymbol{V}_m^T\,\boldsymbol{H}\boldsymbol{B}\boldsymbol{H}^T \qquad (4)$$

where $\boldsymbol{V}_m = (\boldsymbol{v}_i)$ is the matrix of Lanczos vectors $\boldsymbol{v}_i$, which represent the normalized CG search directions, and $\boldsymbol{T}_m = \boldsymbol{V}_m^T\,\boldsymbol{H}\boldsymbol{B}\boldsymbol{H}^T\widetilde{\boldsymbol{P}}\boldsymbol{V}_m$ is a symmetric, positive definite tridiagonal matrix (Gürol *et al.* , 2014). The Lanczos vectors are orthonormal according to $\boldsymbol{V}_m^T\,\boldsymbol{H}\boldsymbol{B}\boldsymbol{H}^T\boldsymbol{V}_m = \boldsymbol{I}_m$ where the norm used is a result of additional restricted preconditioning by $\boldsymbol{B}$ (Gratton and Tshimanga, 2009). The subscript m represents the number of CG iterations performed, referred to as *inner-loops*. In this case, a set of array modes and amplitude coefficients can be defined according to:

$$\widetilde{\boldsymbol{\Psi}}_i = \boldsymbol{B}\boldsymbol{H}^T\boldsymbol{V}_m\boldsymbol{\varphi}_i \qquad (5)$$

$$\tilde{\alpha}_i = \tilde{\lambda}_i^{-1}\boldsymbol{\varphi}_i^T\boldsymbol{V}_m^T\,\boldsymbol{H}\boldsymbol{B}\boldsymbol{H}^T\boldsymbol{R}^{-1}\boldsymbol{d} = \tilde{\lambda}_i^{-1}\widetilde{\boldsymbol{\Psi}}_i^T\boldsymbol{H}^T\boldsymbol{R}^{-1}\boldsymbol{d} \qquad (6)$$

where $(\tilde{\lambda}_i, \boldsymbol{\varphi}_i)$ are the eigenpairs of $\boldsymbol{T}_m$. Since $\widetilde{\boldsymbol{P}}_m$ in (4) represents a reduced-rank approximation of $\boldsymbol{R}^{-1}\boldsymbol{P}$, Moore *et al.* (2018; hereafter MAE) refer to the $\widetilde{\boldsymbol{\Psi}}_i$ as the Reduced-rank Array Modes (RAMs) to distinguish them from the full rank case originally considered by Bennett (1985). It is also important to note that since (5) and (6) are based on the eigen spectrum of the preconditioned matrix $\boldsymbol{R}^{-1}\boldsymbol{P}$, the EOFs of $\widetilde{\boldsymbol{P}}_m$ must be interpreted as the vectors that account for fractions of the *rescaled* total variance in observation. This is also discussed by Le Hénaff *et al.* (2009), who considered a similar rescaling of $\boldsymbol{P}$ by $\boldsymbol{R}^{-1/2}$ and refer to the associated EOFs mapped back into state-space as *modal representers*. In the case considered here, there will be only m RAMs, and the analysis increment can be expressed as $\delta\boldsymbol{x} = \sum_{i=1}^{m} \tilde{\alpha}_i \widetilde{\boldsymbol{\Psi}}_i$.

Despite the differences in definition, several useful complementary interpretations of the array modes and RAMs exist. Bennett (1985) notes that the array modes can be viewed as *interpolation patterns* from observation-space to state-space onto which the observations project. The dependence of the weights $\tilde{\alpha}_i$ on $\tilde{\lambda}_i^{-1}$ dictates that the analysis increments $\delta\boldsymbol{x}$ will be most (least) sensitive to uncertainties in the measurement values that project onto array modes associated with the smallest (largest) eigenvalues. If the eigenvalues $\tilde{\lambda}_i$ are arranged in descending order, then $\widetilde{\boldsymbol{\Psi}}_1$ represents the *most stable* interpolation pattern for the observations into state-space. Conversely, we should treat with caution the $\widetilde{\boldsymbol{\Psi}}_i$ associated with small eigenvalues since these may introduce non-physical noise into the analysis. Viewed another way, the eigen spectrum provides information about the degrees of freedom (*df*) for the signal resolved by the observing array, and the *df* for the noise associated with uncertainties in the observations due to measurement errors and errors of representativeness (Rodgers, 2000). Since $\boldsymbol{R}^{-1}\boldsymbol{HBH}^T$ and $\widetilde{\boldsymbol{P}}$ have the same eigenvectors and their eigenvalues differ by 1, the number of eigenvalues for which $\tilde{\lambda}_i > 2$ provides a measure of the effective number of *df* of the signal that is resolved by the observing array. Array modes associated with $\tilde{\lambda}_i < 2$ will be indistinguishable from errors or uncertainties in the observations (*i.e.* the *df* of the noise in the data) and should be rejected.[1] These ideas have been applied by Bennett and McIntosh (1984), Le Hénaff *et al.* (2009), and MAE to ocean observing systems and will be revisited in section 6 where a more conservative practical criterion is enforced instead of $\tilde{\lambda}_i < 2$ to prevent overfitting to observation errors. Furthermore, since the expected covariance properties of the array mode amplitudes are known *a priori*, identifying the array modes with the *df* provides a useful framework for quantifying the impact of data assimilation on ocean forecasts. These ideas are exploited in section 5.

3 Model Configuration

The ROMS configuration employed in this study spans the MAB and the GoM. Three telescoping nesting layers were used, and the geographical extent of each nested grid is shown in Fig. 1. The model configuration has been described in detail elsewhere (Levin *et al.*, 2019; 2020, 2021), so only a brief description will be given here. The horizontal resolution of the three grids is ~7 km (grid G1), ~2.4 km (grid G2), and ~0.8 km (grid G3), respectively. In all grids, there are 40 terrain-following levels stretched so that the thickness of the surface-most layers is in the

[1] From the definition of $\widetilde{\boldsymbol{P}}_m$ the eigenvalues $\tilde{\lambda}_i \geq 1$ and the lower bound would correspond to the situation where $\boldsymbol{R}^{-1}\boldsymbol{HBH}^T$ is singular.

range 0.1-1.8 m and 0.1-3.4 m near the bottom over the continental shelf. The innermost refined grid, G3, is centered on the NSF OOI Pioneer Array. The G1 open boundaries were constrained using data from the Mercator-Océan real-time global analyses (Lellouche *et al.* 2018) that were adjusted to remove a seasonal bias by comparing with the local, regional climatology derived by Fleming (2016).

Corrections for bias were also made to the G1 open boundary mean dynamic topography and seasonal cycle of sea surface height (SSH) using a regional, data assimilative, climatological analysis as described by Levin *et al.* (2018) and Wilkin *et al.* (2018). Surface fluxes of momentum, heat, and freshwater were derived from 3-hourly National Centers for Environmental Prediction (NCEP) North American Mesoscale (NAM) fields using the standard bulk formulae of Fairall *et al.* (2003). Application of the NAM atmospheric pressure drives an oceanic dynamic inverted barometer response. Daily freshwater discharge from 22 rivers was imposed based on gauge observations from the U.S. Geological Survey and Water Survey of Canada (Lopez *et al.* 2020, Wilkin *et al.* 2018). All three grids can be run using one- or two-way nesting, which provides appropriate boundary conditions for G2 and G3.

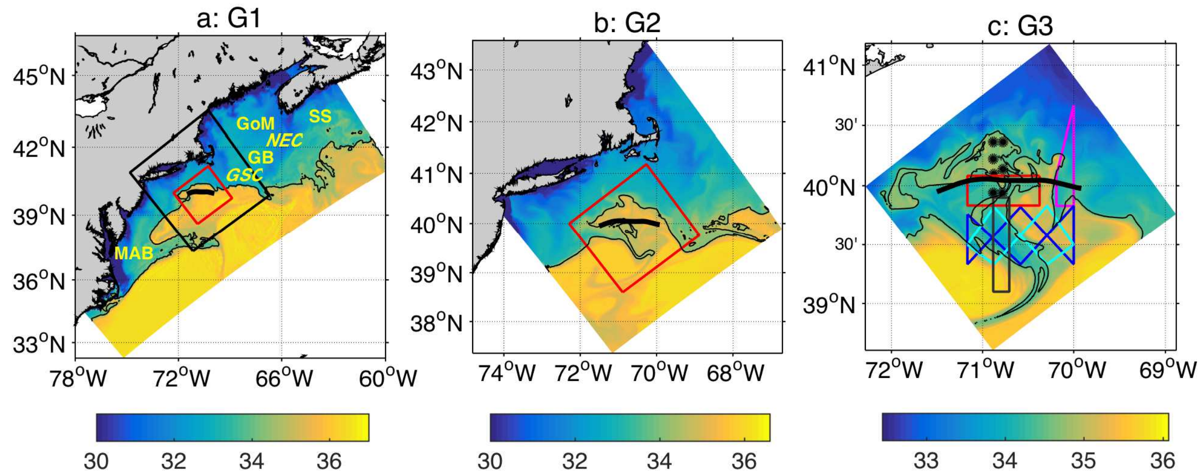

Figure 1: Snapshots of the sea surface salinity on 16 May 2014 from 4D-Var analyses on the three nested grids denoted (a) G1, (b) G2, and (c) G3. The location and extent of grids G2 (black rectangle) and G3 (red rectangle) are shown superimposed on G1 in (a) and G2 in (b). Also shown in (c) are the locations of the Pioneer moorings array (black circles), and the nominal Pioneer glider array (colored lines). The 34.5 isohaline is often used as a proxy for the Mid-Atlantic Bight shelf-break front position and is highlighted in black in each figure. The locations of important geographical features are also shown in (a): GoM=Gulf of Maine, GB=Georges Bank, GSC=Great South Channel, MAB-Mid-Atlantic Bight, NEC=North East Channel, SS=Scotian Shelf (from Levin *et al.*, 2020).

The data assimilation system used is the dual formulation of ROMS 4D-Var (Moore *et al.*, 2011a; Gürol *et al.*, 2014). A full description of the 4D-Var system and its configuration can be found in Levin *et al.* (2018, 2019, 2020, 2021) and Wilkin *et al.* (2018), so only a very brief summary of the salient points is presented here. The data assimilated span the period Jan 2014 - Dec 2017 and are summarized in Table 1 from Levin *et al.* (2020). At the time that these calculations were performed, the ROMS 4D-Var system did not function across one- or two-way nested configurations, so the following strategy was adopted to assimilate the available observations into the three grids:

(i) Data were first assimilated into G1 for the full 2014-2017 period using a 3-day assimilation window. In this case, the model initial conditions, surface forcing, and open boundary conditions were treated as control variables. The background state estimate for each 3-day window was taken to be the analysis at the end of the previous cycle.

(ii) Step (i) was repeated for grid G2, using the 4D-Var analyses from each cycle of G1 as the background open boundary conditions for each 4D-Var cycle of G2. As in G1, the control variables were the initial conditions, surface forcing, and open boundary conditions.

(iii) Step (ii) was then repeated for grid G3. However, in this case, the data assimilation window was reduced to 1-day, with only the initial conditions and open boundary conditions used as control variables. The 4D-Var analyses from each cycle of G2 were used as the background open boundary conditions for each 4D-Var cycle of G3. Also, because of the considerable increase in computational effort, 4D-Var was only run on G3 for the period Jan 2014 – Dec 2015.

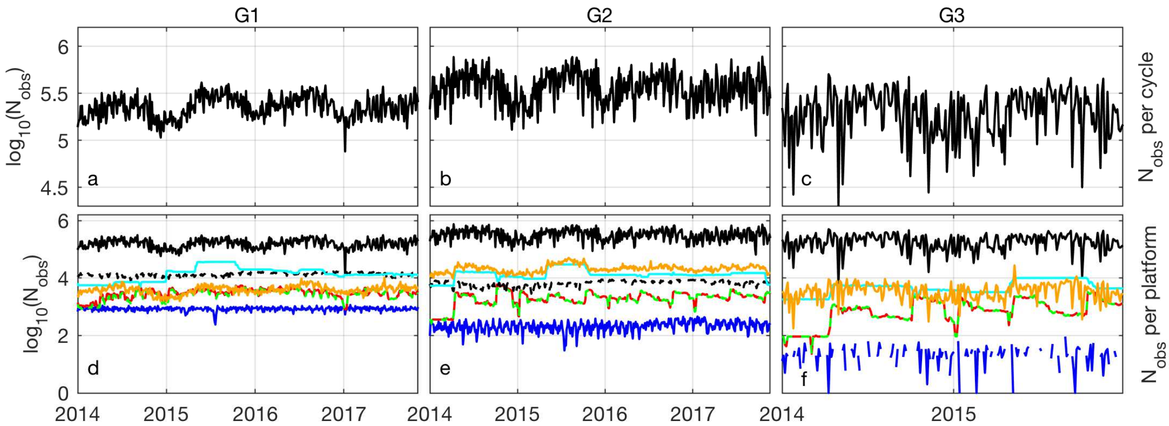

Figure 2: Time series of $\log_{10}$ of the total number of observations (after the formation of super-observations) from *all* platforms assimilated during each 4D-Var cycle on the grid (a) G1, (b) G2, and (c) G3. Time series of the total number of observations from each platform are also shown for (d) G1, (e) G2, and (f) G3: SST – solid black line; SSH – solid blue line; *in situ* temperature – solid red line; *in situ* salinity – green dashed line; gridded HF radar – black dashed line; *in situ* velocity – cyan line; the total number of observations rejected by the background quality control – orange line (from Levin *et al.*, 2020)

Type & platform	**Source**	**Sampling rate and resolution**	**Super-obs averaging[1]**			**Obs error**
			G1	**G2**	**G3**	
AVHRR IR SST	MARACOOS.org & NOAA Coastwatch	4 passes per day, 1 km	3 h	3 h	3 h	σ_b
GOES IR SST	NOAA Coastwatch	Hourly, 6 km	3 h	3 h	3 h	$2\sigma_b$
AMSR2, TRMM and WindSat microwave SST	NASA JPL PO.DAAC	Daily, 15 km	3 h	3 h	3 h	$1.25\sigma_b$
SSH Jason, AltiKa, CryoSat	RADS, TU Delft	~1 pass daily, ~7 km				0.04 m

in situ T, S: NDBC buoys, Argo floats, XBT, surface drifters	Met Office En4.2	Variable[2]	Std.lev[2]	Std.lev[2]	Std.lev[2]	$0.25\sigma_b\sigma_o/\sigma_{max}$[3]
Surface velocity: HF-radar	MARACOOS.org	Hourly, 6 km	24 km	24 km	24 km	$0.5\sigma_b$
in situ T,S: MARACOOS gliders	IOOS Glider DAC	Variable[2]	2 h, Std.lev[2]	1 h, Std.lev[2]	0.33 h, Std.lev[2]	$0.25\sigma_b\sigma_o/\sigma_{max}$[3]
in situ T,S: Gulf of Maine	NERACOOS.org[4]	Hourly, 10 buoys				σ_b
in situ u,v: Gulf of Maine		Hourly, 9 buoys[1]				$0.5\sigma_b$
in situ T,S: Pioneer moorings	NSF Ocean Observatories Initiative[7]	~3 h profiles, 7 moorings[5] ~60% data availability[6]	2 h, Std.lev[2]	2 h, Std.lev[2]	0.33 h, Std.lev[2]	$0.25\sigma_b\sigma_o/\sigma_{max}$[3]
in situ T,S: Pioneer gliders		Variable[2] ~4 h, ~4 km	2h, Std.lev[2]	2h, Std.lev[2]	0.33 h, Std.lev[2]	$0.25\sigma_b\sigma_o/\sigma_{max}$[3]
in situ u,v: Pioneer moorings		30 min, ~75% data availability[6]	Std.lev[2]	Std.lev[2]	Std.lev[2]	$0.5\sigma_b$

Table 1: A summary of the observational data assimilated into ROMS during 2014–2017, the procedure for forming super-observations, and the observation errors assigned to each observation type (from Levin *et al.,* 2020). In the final column, σ_o and σ_b denote the standard deviation of observation errors and background errors, respectively; the formulae given are the scaling relationships used for the indicated observation types. The superscripts provide additional information. 1: All data sampled at a horizontal resolution higher than that of the model were formed into super observations at the resolution of the ROMS grid unless otherwise indicated. 2: Profile data were binned in the vertical using the World Ocean Data atlas standard depths (Boyer *et al.*, 2009). 3: Here, σ_o is the standard deviation of all observations that fall within a vertical bin (see comment 1), and σ_{max} is the maximum value of all σ in a vertical profile. 4: NERACOOS = North East Regional Association Coastal Ocean Observing System. 5: Moorings 2 and 4 deployed in November 2017. 6: Average over 2014-2017. 7: Data downloaded from NSF OOI Data Portal http://ooinet.oceanobservatories.org and aggregated by platform at www.myroms.org:8080/erddap/info.

As discussed in Moore *et al.* (2011a), the background error covariance $\boldsymbol{B}$ matrix in ROMS is modeled following the diffusion operator approach of Weaver and Courtier (2001). Table 2 summarizes the decorrelation length scales assumed in $\boldsymbol{B}$ for errors in each control variable on the three model grids used here, and these parameter choices are discussed in Levin *et al.* (2019).

State variable	**Horizontal decorrelation scale (km) (G1|G2|G3)**	**Background quality control parameter γ (G1|G2|G3)**
SSH	40 | 14 | 5	5 | 5 | ∞
Velocity	40 | 14 | 5	1.5 | 1.5 | ∞
Temperature	15 | 14 | 5	6 | 6 | 6
Salinity	15 | 14 | 5	12 | 12 | 12
Surface forcing	100 | 100 | -	-

Table 2: A summary of the decorrelation scales assumed for background errors in each control variable on all three grids. The vertical decorrelation length scale for all state variables of the initial conditions and open boundary

conditions was chosen to be 10 m. In the case of the surface forcing, the same horizontal decorrelation lengths were imposed on all fields. The parameter γ used for the background quality control rejection criteria is also indicated: $\gamma = \infty$ indicates that no background quality control check was applied to these data. A dash in any column indicates that the parameter is not applicable.

The observation error covariance matrix $\boldsymbol{R}$ was assumed to be a diagonal matrix, and Table 1 summarizes the errors and uncertainties that were assigned to measurements from each observing platform. These errors reflect a combination of measurement error and errors of representativeness (*i.e.*, uncertainties associated with the ability of the model grid to resolve all of the processes that are captured by the observations) and are also discussed in Levin *et al.* (2019). Following Andersson and Järvinen (1999), quality control was performed during each 4D-Var cycle. Specifically, the innovation d_i associated with each observation is compared to the standard error based on the assumed standard deviations of the background (σ_b) and observation (σ_o) errors. For a chosen threshold γ, an observation is rejected and not included in the analysis if $d_i^2 > \gamma^2(\sigma_b^2 + \sigma_o^2)$. The thresholds γ depend on the type of observation and are given in Table 2 for the analyses on each grid considered here.

Time series of the total number of observations assimilated into the model on each grid (after the formation of super observations) during a 4D-Var cycle are shown in Fig. 2. Also shown are time series of the number of observations from each observing platform. The number of observations from each platform is similar across all three grids, apart from satellite altimetry. The number of altimeter overpasses decreases dramatically, going from G1 to G3 due to the reduced geographical extent of each nested grid.

The performance of the 4D-Var system on each of the three grids has been documented in detail by Levin *et al.* (2019, 2020, 2021). Suffice to say, the system performs well across all three grids, and interested readers are encouraged to refer to these previous studies for more details. An example 4D-Var analysis from each grid is illustrated in Fig. 1, which shows sea surface salinity on 16 May 2014. At this time, a streamer of saline water associated with a large Gulf Stream eddy can be seen impinging on the shelf, an event that has been studied in detail by Zhang and Gawarkiewicz (2015). Figure 1 shows very clearly how the 4D-Var circulation estimates can capture the range of scales from quasi-geostrophic down to the sub-mesoscale secondary circulations as the grid resolution increases.

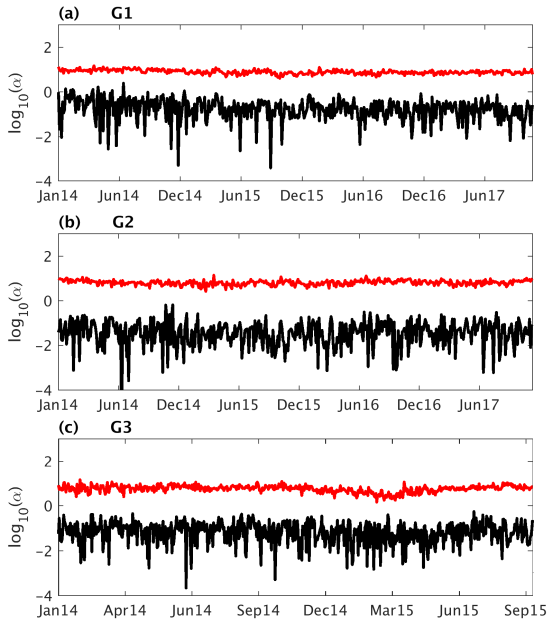

Figure 3: Time series of the RAM amplitudes $\log_{10}(|\tilde{\alpha}_1|)$ (black line) and $\log_{10}(|\tilde{\alpha}_7|)$ (red line) associated with the 1st outer-loop of each 4D-Var analysis cycle for (a) G1, (b) G2, and (c) G3.

4 Reduced Rank Array Modes

The incremental 4D-Var procedure outlined in section 2 is equivalent to minimizing a *cost function* that represents the squared difference between $\boldsymbol{x}^a$ and $\boldsymbol{x}^b$, and the observations and $\boldsymbol{x}^a$ evaluated at the space-time observation locations, weighted by the inverse background error and observation error covariance matrices respectively (*e.g.*, Courtier *et al*., 1994). The desired best, linear, unbiased, estimate is given by (1), and, as outlined in section 2, can be identified using CG methods via a sequence of inner-loop iterations. In keeping with the usual practice, the incremental formulation of 4D-Var adopted in ROMS also employs an outer-loop, and the ocean state about which $\boldsymbol{H}$ and $\boldsymbol{H}^T$ are linearized is updated after every m inner-loops. The ROMS 4D-Var analyses described in section 3 were computed using two outer-loops and seven inner-loops, in which case $\boldsymbol{x}^a = \boldsymbol{x}^b + \delta\boldsymbol{x}_1 + \delta\boldsymbol{x}_2$ where the subscript refers to the contribution from each outer-loop. In this case, each $\delta\boldsymbol{x}$ can be expanded in terms of the RAMs appropriate for the outer-loop under consideration. Levin *et al.* (2020) showed that it is in the 1st outer-loop that increments are largest and where the observations have the greatest impact on the final analysis. Therefore, in the sequel, we will focus on the RAMs of the first outer-loop for the 4D-Var analyses of section 3. In addition, we will demonstrate in section 5 how the RAMs can be used to quantify the influence of data assimilation on the expected forecast errors, and there, for mathematical convenience, we will focus on a single 4D-Var outer-loop.

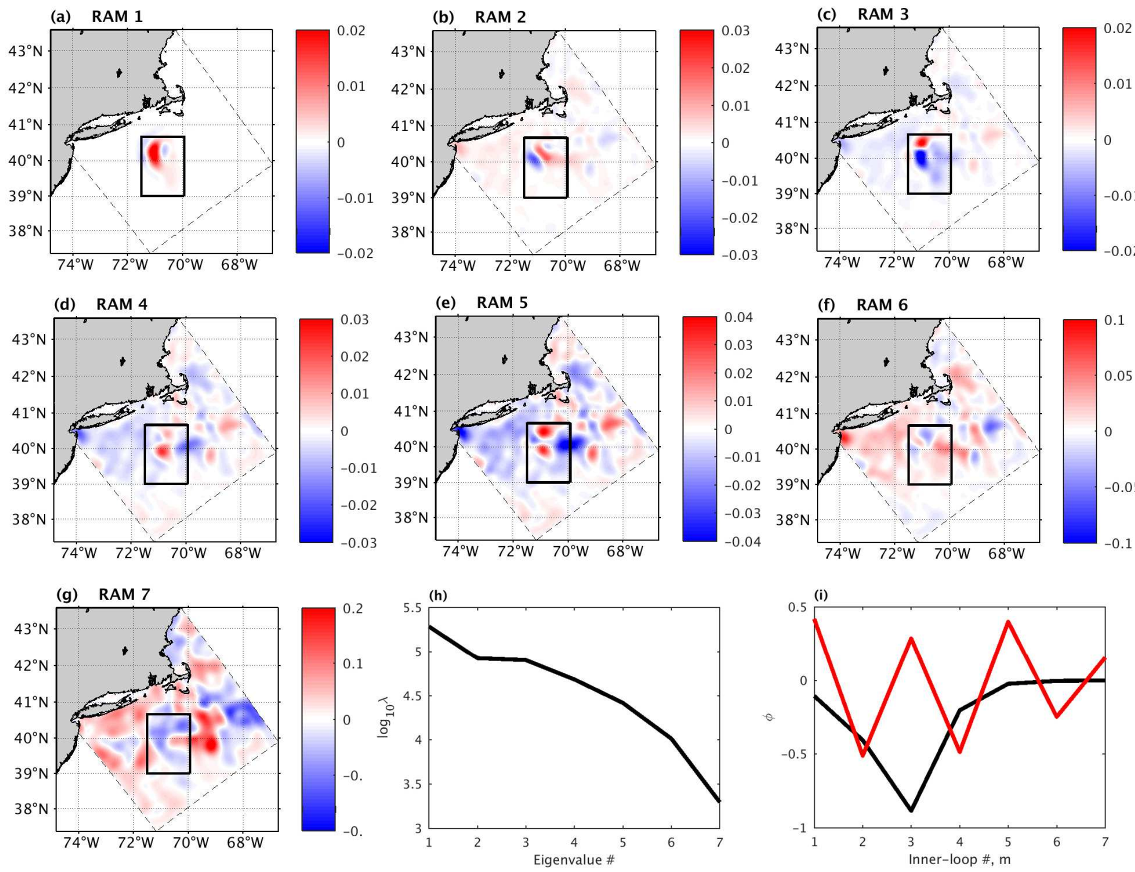

Figure 4: The SST components of each RAM are shown in (a)-(g) for G2 from the 1st outer-loop of the 4D-Var cycle starting on 17 Sept 2015. The nominal extent of the Pioneer glider array is also indicated (black box), and the units are °C. The thin dashed line indicates the extent of the model grid. (h) The eigen spectrum $\tilde{\lambda}_i$ of the 1st outer-loop for the same 4D-Var cycle. (i) The eigenvector $\boldsymbol{\varphi}_1$ (black line) and $\boldsymbol{\varphi}_7$ (red line) for the same 4D-Var cycle. Both (h) and (i) are unitless.

Following (5) and (6) and recalling that $m = 7$ for the 4D-Var analyses considered here, there will be seven RAMs for each outer-loop. Figure 3 shows time series of $|\tilde{\alpha}_1|$ and $|\tilde{\alpha}_7|$, the absolute value of the amplitudes of the RAMs associated with the largest eigenvalue $\tilde{\lambda}_1$ and smallest eigenvalue $\tilde{\lambda}_7$ of $\widetilde{\boldsymbol{P}}_m$for the 1st outer-loop of each 4D-Var cycle in the three grids. On average, $|\tilde{\alpha}_7|/|\tilde{\alpha}_1|$ varies in the range ~10-10^3, although there are some cycles where the ratio can be as high as 10^5. Therefore, errors and uncertainties in the innovations $\boldsymbol{d}$ that project onto RAM $\widetilde{\boldsymbol{\Psi}}_7$ will have considerably more influence on the analysis increments than those that project onto RAM $\widetilde{\boldsymbol{\Psi}}_1$.

To illustrate the typical structure of the RAMs, Fig. 4 shows the sea surface temperature (SST) associated with each RAM of the 1st outer-loop for the 3-day 4D-Var cycle spanning the interval 17-19 Sept 2015 on G2. Specifically, Fig. 4 shows the RAM SST on 17 Sept at the beginning of the assimilation cycle. RAMs $\widetilde{\boldsymbol{\Psi}}_1$ (Fig. 4a), $\widetilde{\boldsymbol{\Psi}}_2$ (Fig. 4b) and $\widetilde{\boldsymbol{\Psi}}_3$ (Fig. 4c) have largest amplitude in the vicinity of the Pioneer Array. Conversely, RAMs $\widetilde{\boldsymbol{\Psi}}_4$ through $\widetilde{\boldsymbol{\Psi}}_7$ generally have more complicated SST structures that span a larger portion of the model domain. The eigenvalue spectrum of $\widetilde{\boldsymbol{P}}_m$ for this 4D-Var cycle is shown in Fig. 4h and spans about two orders of magnitude.

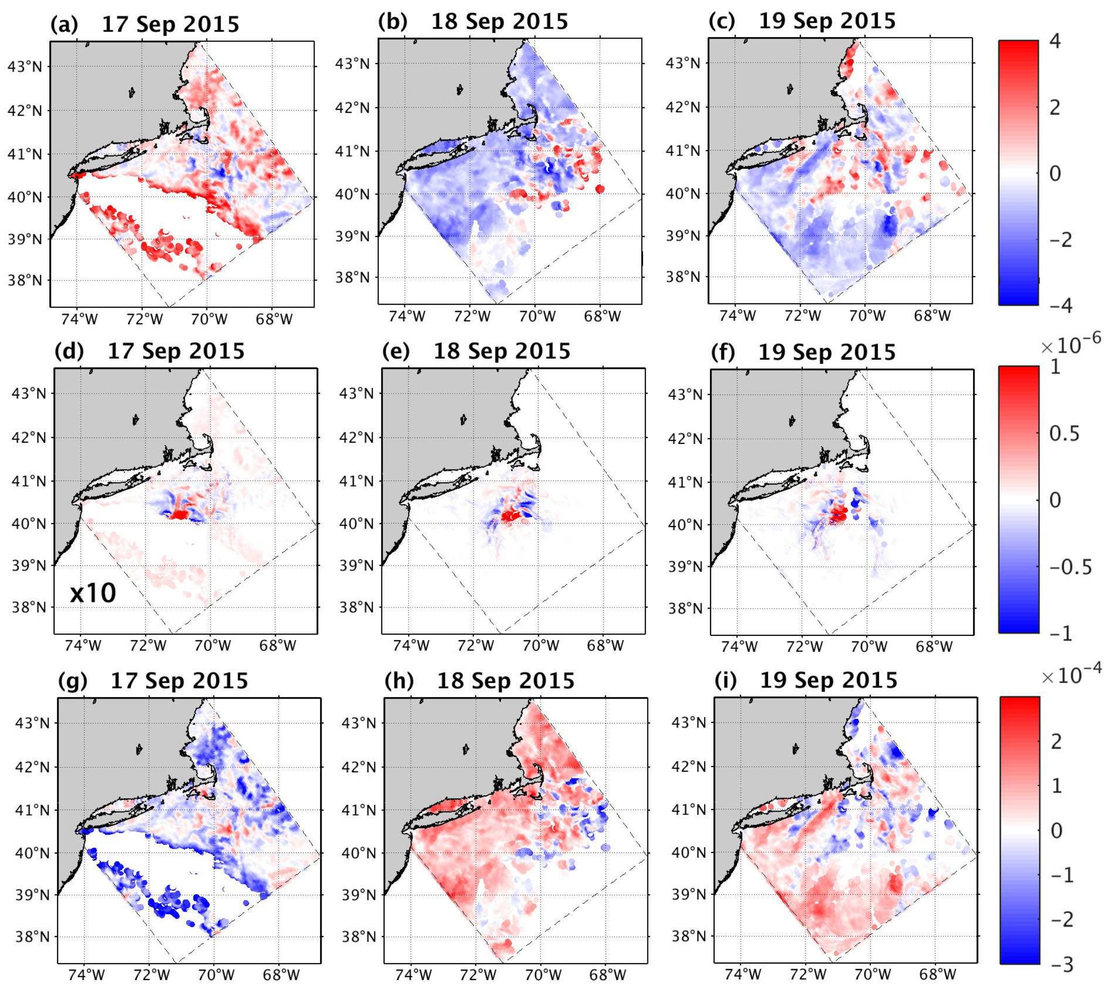

Figure 5: The SST innovations for three separate AVHRR overpasses are shown in (a)-(c). The corresponding SST components of $\boldsymbol{V}_m\boldsymbol{\varphi}_1$ are shown in (d)-(f) and those for $\boldsymbol{V}_m\boldsymbol{\varphi}_7$ in (g)-(i) on the same days. Units are °C in all panels. The thin dashed line indicates the extent of the model grid. Note that panel (d) is scaled by a factor of 10 for convenience.

It is important to reiterate that the RAMs do *not* depend on the observation values, only on their locations (in concert with the background state and the error covariances). To illustrate this aspect of the RAMS, Fig. 4i shows the structure of $\boldsymbol{\varphi}_1$ and $\boldsymbol{\varphi}_7$, the leading and trailing eigenvectors of the Lanczos decomposition of the inner-loop iterations, during the same G2 assimilation cycle. According to (5), the leading and trailing RAMs are given by $\widetilde{\boldsymbol{\Psi}}_1 = \boldsymbol{B}\boldsymbol{H}^T\boldsymbol{V}_m\boldsymbol{\varphi}_1$ and $\widetilde{\boldsymbol{\Psi}}_7 = \boldsymbol{B}\boldsymbol{H}^T\boldsymbol{V}_m\boldsymbol{\varphi}_7$ representing the projection of $\boldsymbol{\varphi}_1$ and $\boldsymbol{\varphi}_7$ in Fig. 4i into state-space. Specifically, the elements of $\boldsymbol{\varphi}_1$ and $\boldsymbol{\varphi}_7$ represent weights for the Lanczos vectors that form the columns of $\boldsymbol{V}_m$. The weighted sums of the Lanczos vectors $\boldsymbol{V}_m\boldsymbol{\varphi}_1$ and $\boldsymbol{V}_m\boldsymbol{\varphi}_7$ are then mapped into state-space by the adjoint observation operator $\boldsymbol{H}^T$, which in 4D-Var involves an integration backwards in time. After the mapping into state-space, the state-vector is multiplied by the background error covariance $\boldsymbol{B}$ which has the effect of smoothing the fields according to the decorrelation length scales assumed in Table 2. The smooth nature of the RAM SST in Figs. 4a and 4g is very evident for these two modes.

During the 17-19 Sept 2015 4D-Var cycle, the most abundant observations are SST from several different platforms. Figures 5a-c show the innovations associated with three separate overpasses of the AVHRR instrument on different days, while Figs. 5d-f show the elements of $\boldsymbol{V}_m\boldsymbol{\varphi}_1$ associated with the same observations. There is little or no correspondence between the innovations in Figs. 5a-c and the image of $\boldsymbol{\varphi}_1$ mapped into state-space shown in Figs. 5d-f. However, the SST structure of the associated RAM $\widetilde{\boldsymbol{\Psi}}_1$ (cf. Fig. 4a) is already evident in Figs. 5d-f. Conversely, Figs. 5g-i show the elements of $\boldsymbol{V}_m\boldsymbol{\varphi}_7$ at the AVHRR observation locations, and some features of RAM $\widetilde{\boldsymbol{\Psi}}_7$ (cf. Fig. 4g) are already apparent. Thus, the absence of any general correspondence between the RAM structures and the innovations further illustrates the their independence from the observation values.

The structure of RAM $\widetilde{\boldsymbol{\Psi}}_1$ appears to be closely aligned with the location of the *in situ* observations. For example, Fig. 6 shows the 3-dimensional temperature structure of $\widetilde{\boldsymbol{\Psi}}_1$ on 17 Sept 2015 on G2 in the vicinity of the Pioneer mooring array, and the region of the ocean informed by the RAM appears to be closely aligned with some of the *in situ* mooring observations. The same is true for the other state-vector components of RAM $\widetilde{\boldsymbol{\Psi}}_1$ (not shown).

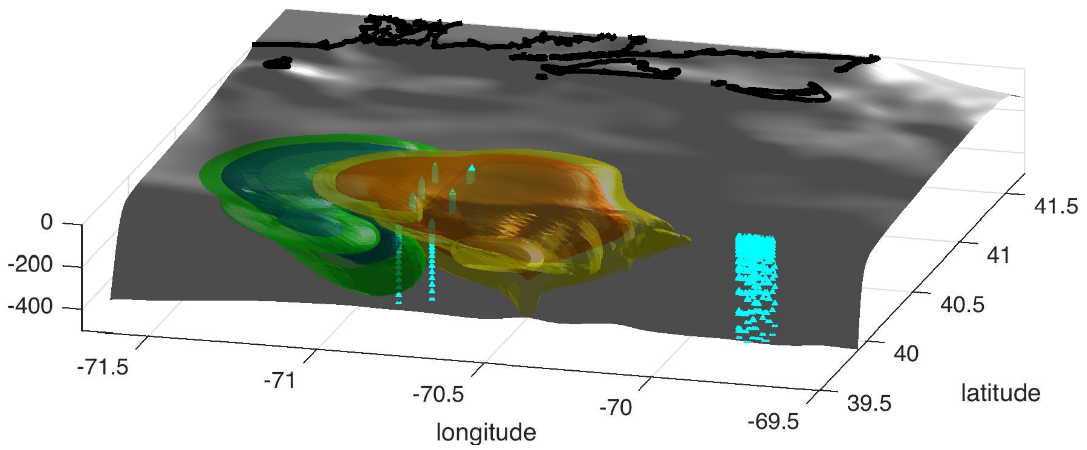

Figure 6: The close-up of the 3-dimensional structure of the $\widetilde{\boldsymbol{\Psi}}_1$ upper-ocean temperature field on 17 Sept 2015 for G2 in the vicinity of the Pioneer mooring array. The color scale is as follows: blue = -0.3°C, green = -0.1°C, yellow = 0.1°C, red = 0.2°C. The cyan triangles indicate the location of the *in situ* observations during the 4D-Var cycle.

The contribution of each RAM to the 4D-Var increment is given by $\tilde{\alpha}_i\widetilde{\boldsymbol{\Psi}}_i$, and according to Fig. 3, it is anticipated that $\widetilde{\boldsymbol{\Psi}}_7$ will contribute the most. This is confirmed in Fig. 7, which shows the root mean square (RMS) of SST averaged over all 4D-Var cycles on each grid associated with $\widetilde{\boldsymbol{\Psi}}_1$ and $\widetilde{\boldsymbol{\Psi}}_7$. RAM $\widetilde{\boldsymbol{\Psi}}_7$ clearly dominates, which is also the case at depth and for other fields (not shown). Thus, much of the detailed structure in the analysis increments is associated with the trailing RAMs. It is important to note that while the $\boldsymbol{\varphi}_i$ are orthogonal, the RAMs are not, so Fig.

7 *cannot* be interpreted as the contribution of $\widetilde{\boldsymbol{\Psi}}_1$ and $\widetilde{\boldsymbol{\Psi}}_7$ to the total SST variance of the increments.

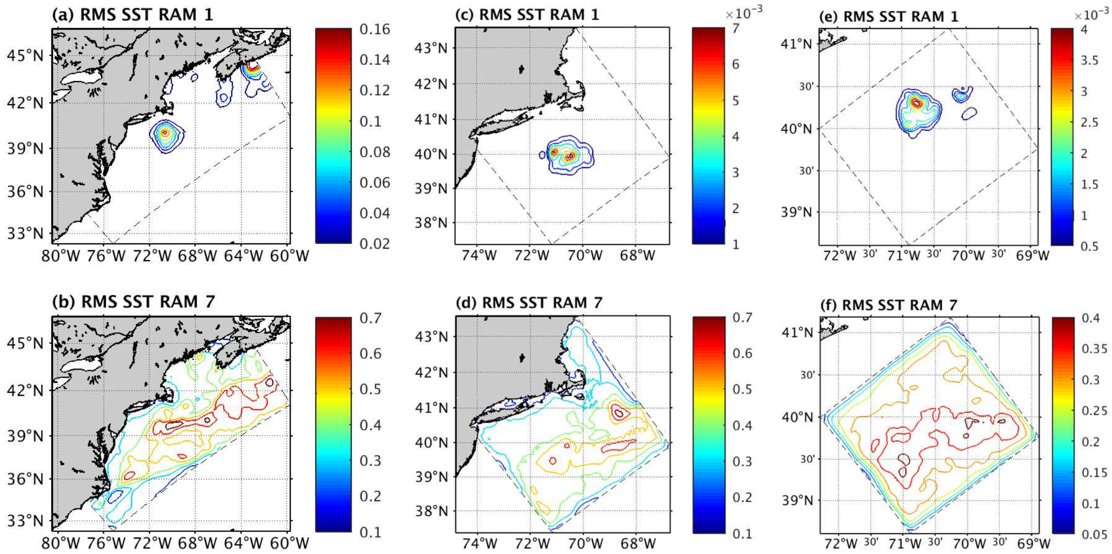

Figure 7: The RMS SST (°C) of $\tilde{\alpha}_1\widetilde{\boldsymbol{\Psi}}_1$ (top row) and $\tilde{\alpha}_7\widetilde{\boldsymbol{\Psi}}_7$ (bottom row) averaged over all 4D-Var cycles for (a,b) G1, (c,d) G2, and (e,f) G3. Units are °C in all panels. The thin dashed line indicates the extent of each model grid.

It is important to note that the RAMs comprise components that are associated with all elements of the 4D-Var control vector. Therefore, in the case of G1 and G2, this includes fields of surface flux forcing and for the open boundary conditions in the case of all three grids. In the interest of brevity, we will not discuss these additional components of the RAMs here.

Taken together, Figs. 4 and 7 indicate that the leading RAMs of G2 appear to be primarily associated with the Pioneer Array. In contrast, the trailing RAMs span most of the model domain and are largely controlled by the location of remote sensing footprints. The RAMs of G1 also confirm this picture (not shown). However, as demonstrated in section 6, this view is an oversimplification.

5 The Impact of Data Assimilation on Expected Forecast Uncertainty

5.1 Analysis and forecast error covariance

As discussed in section 2, the RAMs can be interpreted as *interpolation patterns* for the innovations into state-space and provide quantitative information about the sensitivity of the analysis increments to measurement errors and errors of representation (see also section 6). This idea can be exploited further to quantify the expected errors in analyses and subsequent forecasts that arise from uncertainties in the *innovations*. The analysis increment at the beginning of the 4D-Var analysis cycle is given by $\delta\boldsymbol{x} = \boldsymbol{K}\boldsymbol{d} = \sum_{i=1}^{m}\tilde{\alpha}_i\widetilde{\boldsymbol{\Psi}}_i$. Therefore, uncertainty in the observations and background will manifest as uncertainties in the innovation vector $\boldsymbol{d}$, which enter through the 2nd equality as uncertainties in $\tilde{\alpha}_i$, according to (6). For the best, linear, unbiased estimate $E\{\delta\boldsymbol{x}\} = \boldsymbol{0}$, where $E\{\cdots\}$ is the expectation operator. Similarly, the expected covariance of the increments associated with uncertainties in $\boldsymbol{d}$ is given by $\boldsymbol{C} = E\{\delta\boldsymbol{x}\delta\boldsymbol{x}^T\} = \boldsymbol{K}E\{\boldsymbol{d}\boldsymbol{d}^T\}\boldsymbol{K}^T = \boldsymbol{B} - \boldsymbol{A}$, where $\boldsymbol{A}$ is the expected analysis error covariance (Daley, 1991).[2] Hence, $\boldsymbol{C}$ represents the *reduction* in the background error covariance due to assimilating the observations since $\|\boldsymbol{A}\| < \|\boldsymbol{B}\|$ for any norm (see footnote 2). Expressing $\delta\boldsymbol{x}$ in terms of the RAMs, it can be shown that[3]:

$$\boldsymbol{C} = \sum_{i=1}^{m}\left(1 - \tilde{\lambda}_i^{-1}\right)\widetilde{\boldsymbol{\Psi}}_i\widetilde{\boldsymbol{\Psi}}_i^T \qquad (7)$$

using the expected covariance properties of $\boldsymbol{d}$. At the end of the 4D-Var analysis window, the analysis increment is well approximated by $\boldsymbol{M}\delta\boldsymbol{x}$, where $\boldsymbol{M}$ represents the tangent linear model linearized about the time-evolving background state-vector. Therefore, (7) can also be used to compute the expected error variance, $\boldsymbol{MCM}^T = \boldsymbol{MBM}^T - \boldsymbol{MAM}^T$, at the *end* of the analysis cycle by merely replacing each RAM $\widetilde{\boldsymbol{\Psi}}_i$ in (7) by the time evolved RAMs $\boldsymbol{M}\widetilde{\boldsymbol{\Psi}}_i$. During the analysis cycle, the surface forcing and open boundary condition components of $\widetilde{\boldsymbol{\Psi}}_i$ are also used as inputs for $\boldsymbol{M}$. The 4D-Var analysis at the end of the assimilation window is commonly used as the initial condition for a forecast. Similarly, the 4D-Var increments $\delta\boldsymbol{x}$ can be propagated into the forecast interval using $\boldsymbol{M}$ linearized about the 4D-Var background (also extended into the forecast interval), and subject to the appropriate forecast boundary conditions and surface forcing.

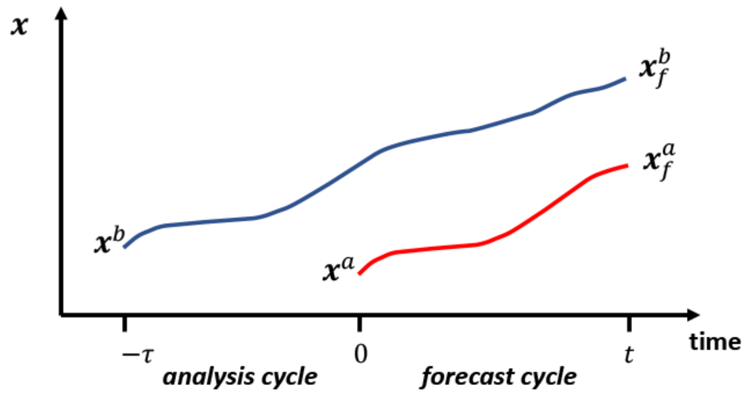

Figure 8: A schematic showing a typical analysis and forecast cycle. The background for the 4D-Var analysis cycle spanning the interval $[-\tau, 0]$ is denoted as $\boldsymbol{x}^b$. 4D-Var yields an estimate of the ocean state denoted $\boldsymbol{x}^a(0)$, which can be used as the initial condition for a forecast over the interval $[0, t]$. The forecast state resulting from the 4D-Var

---

[2] From the expected covariance of the innovation vector $\boldsymbol{C} = \boldsymbol{K}E\{\boldsymbol{d}\boldsymbol{d}^T\}\boldsymbol{K}^T = \boldsymbol{K}(\boldsymbol{HBH}^T + \boldsymbol{R})\boldsymbol{K}^T$, and, using (2) $\boldsymbol{C} = \boldsymbol{KHB}$. The analysis error covariance matrix $\boldsymbol{A} = (\boldsymbol{I} - \boldsymbol{KH})\boldsymbol{B}$ which shows that $\|\boldsymbol{A}\| < \|\boldsymbol{B}\|$ for any norm, and furthermore, $\boldsymbol{B} - \boldsymbol{A} = \boldsymbol{KHB} = \boldsymbol{C}$.

[3] The increment $\delta\boldsymbol{x} = \sum_{i=1}^{m}\tilde{\alpha}_i\widetilde{\boldsymbol{\Psi}}_i$ so that $\boldsymbol{C} = E\{\delta\boldsymbol{x}\delta\boldsymbol{x}^T\} = E\left\{\sum_{i=1}^{m}\sum_{j=1}^{m}\tilde{\alpha}_i\tilde{\alpha}_j\widetilde{\boldsymbol{\Psi}}_i\widetilde{\boldsymbol{\Psi}}_j^T\right\} = \sum_{i=1}^{m}\sum_{j=1}^{m}E\left\{\tilde{\alpha}_i\tilde{\alpha}_j\right\}\widetilde{\boldsymbol{\Psi}}_i\widetilde{\boldsymbol{\Psi}}_j^T$. Using (6), $E\left\{\tilde{\alpha}_i\tilde{\alpha}_j\right\} = \tilde{\lambda}_i^{-1}\tilde{\lambda}_j^{-1}\boldsymbol{\varphi}_i^T\boldsymbol{V}_m^T\,\boldsymbol{HBH}^T\boldsymbol{R}^{-1}\,\boldsymbol{K}E\{\boldsymbol{d}\boldsymbol{d}^T\}\boldsymbol{R}^{-1}\boldsymbol{HBH}^T\boldsymbol{V}_m\boldsymbol{\varphi}_j$. From (4), $E\{\boldsymbol{d}\boldsymbol{d}^T\} = \boldsymbol{R}\boldsymbol{V}_m\boldsymbol{T}_m\boldsymbol{V}_m^T\,\boldsymbol{HBH}^T$, and recalling that $\boldsymbol{V}_m^T\,\boldsymbol{HBH}^T\boldsymbol{V}_m = \boldsymbol{I}_m$ we can write $E\left\{\tilde{\alpha}_i\tilde{\alpha}_j\right\} = \tilde{\lambda}_i^{-1}\tilde{\lambda}_j^{-1}\boldsymbol{\varphi}_i^T\boldsymbol{T}_m\boldsymbol{V}_m^T\,\boldsymbol{HBH}^T\boldsymbol{R}^{-1}\boldsymbol{HBH}^T\boldsymbol{V}_m\boldsymbol{\varphi}_j$. Recall that $\boldsymbol{T}_m\boldsymbol{\varphi}_i = \tilde{\lambda}_i\boldsymbol{\varphi}_i$ and that the symmetric tridiagonal matrix $\boldsymbol{T}_m \equiv \boldsymbol{V}_m^T\,\boldsymbol{HBH}^T(\boldsymbol{R}^{-1}\boldsymbol{HBH}^T + \boldsymbol{I})\boldsymbol{V}_m$, in which case $E\left\{\tilde{\alpha}_i\tilde{\alpha}_j\right\} = \tilde{\lambda}_j^{-1}\boldsymbol{\varphi}_i^T(\boldsymbol{T}_m - \boldsymbol{I}_m)\boldsymbol{\varphi}_j = \tilde{\lambda}_j^{-1}\left(\tilde{\lambda}_i - 1\right)\boldsymbol{\varphi}_i^T\boldsymbol{\varphi}_j = \tilde{\lambda}_j^{-1}\left(\tilde{\lambda}_i - 1\right)\delta_{i,j}$, where $\delta_{i,j}$ is the Kronecker delta-function. Therefore, $E\left\{\tilde{\alpha}_i\tilde{\alpha}_j\right\} = \left(1 - \tilde{\lambda}_i^{-1}\right)\delta_{i,j}$ and $\boldsymbol{C} = \sum_{i=1}^{m}\left(1 - \tilde{\lambda}_i^{-1}\right)\widetilde{\boldsymbol{\Psi}}_i\widetilde{\boldsymbol{\Psi}}_i^T$.

analysis is denoted $\boldsymbol{x}_f^a$. If the 4D-Var background is extended through the forecast interval, this yields a second forecast $\boldsymbol{x}_f^b$, and the difference $\boldsymbol{x}_f^b - \boldsymbol{x}_f^a$ represents the impact of data assimilation on the forecast.

While an estimate of the expected analysis error covariance matrix $\boldsymbol{MAM}^T$ at the end of the analysis cycle is desirable, it is challenging to compute in 4D-Var (*e.g.,* Fisher and Courtier, 1995; Ngodock *et al.*, 2020; Moore and Arango, 2021), one reason being that the contribution of the background error covariance $\boldsymbol{MBM}^T$ is computationally demanding to calculate. Reduced-rank estimates are one approach, although they tend to underestimate the analysis errors (Fisher and Courtier, 1995; Moore *et al.*, 2011b). Ngodock *et al.* (2020) have demonstrated a Monte Carlo approach for estimating $\boldsymbol{A}$ based on computing an ensemble of 4D-Var analyses by perturbing the so-called "representer coefficients" $\boldsymbol{\beta} = (\boldsymbol{HBH}^T + \boldsymbol{R})^{-1}\boldsymbol{d}$. This approach is related to that used here. However, in our case, we capitalize on the known covariance properties of the RAM amplitudes in (7) without the need to compute an explicit ensemble of analyses and forecasts. In the case of the expected forecast error covariance, some additional computational cost is involved since each RAM (or equivalently each Lanczos vector $\boldsymbol{v}_i$) must be propagated to the end of the forecast interval using the tangent linear model $\boldsymbol{M}$. Since the computational cost of $\boldsymbol{M}$ in ROMS is about 50% more than a run of the nonlinear forecast model, then, for forecast lead times that are similar in length to the assimilation window, the additional calculations required are $\sim 1.5m$ where m is the number inner-loops (and of course the number of RAMs). In the examples here $m = 7$, so the additional computational burden is equivalent to running an O(10) ensemble of forecasts. This is much smaller than the ensemble size required to estimate $\boldsymbol{MAM}^T$ using, say, the randomization method of Fisher and Courtier (1995) in which a sample size ~5000 would be needed to yield an estimate of the leading diagonal accurate to ~1%.

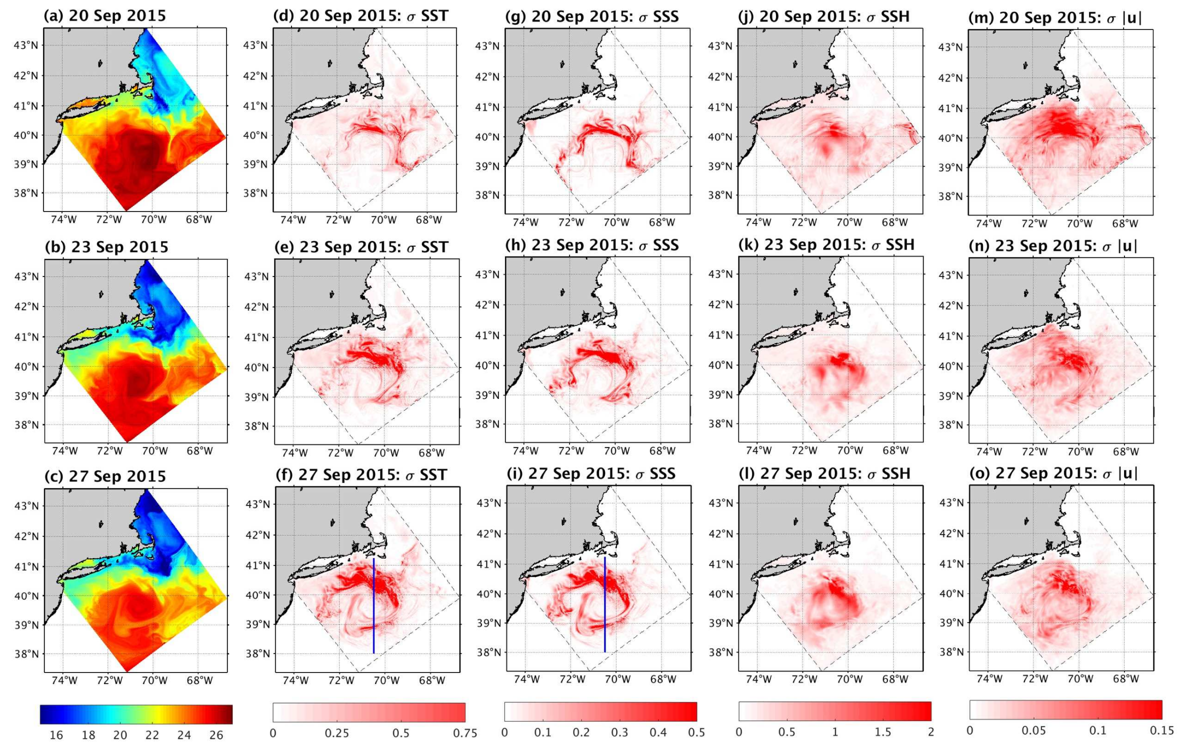

Figure 9: The G2 4D-Var background SST (°C) used as the $\boldsymbol{x}_f^b$ forecast initial condition on 20 Sept 2015 is shown in (a). The 3-day and 7-day forecast SST fields of $\boldsymbol{x}_f^b$ are shown in (b) and (c), respectively. The *standard deviations* given by the square-root of the diagonal elements of $\boldsymbol{M}(-\tau,t)\boldsymbol{C}\boldsymbol{M}^T(t,-\tau)$ for SST (°C) are shown for the same dates in (d), (e), and (f). The corresponding *standard deviations* for the forecasts of SSS (g,h,i), SSH (cm) (j,k,l) and surface current speed (ms^{-1}) (m,n,o) are also shown. The blue lines in (f) and (i) represent the location of the vertical sections along 70.5°W shown in Fig. 10.

To illustrate the utility of our approach, consider the two forecasts illustrated schematically in Fig. 8. Forecast $\boldsymbol{x}_f^a(t)$ is initialized from the analysis $\boldsymbol{x}^a(0)$ at the end of each 4D-Var analysis cycle, while forecast $\boldsymbol{x}_f^b(t)$ is initialized from the background $\boldsymbol{x}^b(-\tau)$ of the 4D-Var cycle. The forecast $\boldsymbol{x}_f^a(t)$, therefore, benefits from the data that were assimilated during the 4D-Var cycle spanning the interval $[-\tau, 0]$, while forecast $\boldsymbol{x}_f^b(t)$ does not. The expected forecast error covariances of $\boldsymbol{x}_f^a(t)$ and $\boldsymbol{x}_f^b(t)$ are given by $\boldsymbol{M}(-\tau,t)\boldsymbol{A}\boldsymbol{M}^T(t,-\tau)$ and $\boldsymbol{M}(-\tau,t)\boldsymbol{B}\boldsymbol{M}^T(t,-\tau)$ respectively, where the ordering of the time arguments indicates the direction of integration. Therefore, $\boldsymbol{M}(-\tau,t)\boldsymbol{C}\boldsymbol{M}^T(t,-\tau) = \boldsymbol{M}(-\tau,t)\boldsymbol{B}\boldsymbol{M}^T(t,-\tau) - \boldsymbol{M}(-\tau,t)\boldsymbol{A}\boldsymbol{M}^T(t,-\tau)$ represents the change in the forecast error covariance associated with assimilating the observations. Since the covariance information is propagated using $\boldsymbol{M}(-\tau,t)$, the resulting covariance matrices represent 1^{st}-order approximations.

Following this approach, forecasts were initialized at the end of the 1^{st} outer-loop of each 3-day 4D-Var cycle on G1 and G2 respectively for the period 1 Jan – 31 Dec 2015. The forecast duration was 10-days for G1 and 7-days for G2. A longer forecast interval was used in G1 because of the larger geographical extent of the model domain. For such extended forecast periods, true forecast fields are not available for the NCEP-NAM surface forcing. Therefore, for convenience, a best time series concatenation of the 1-day forecast NCEP-NAM meteorology and Mercator-Océan open boundary data were used during these forecast experiments. In the near real-time MARACOOS system for G1, true 3-day forecast products from the respective operational centers are employed.

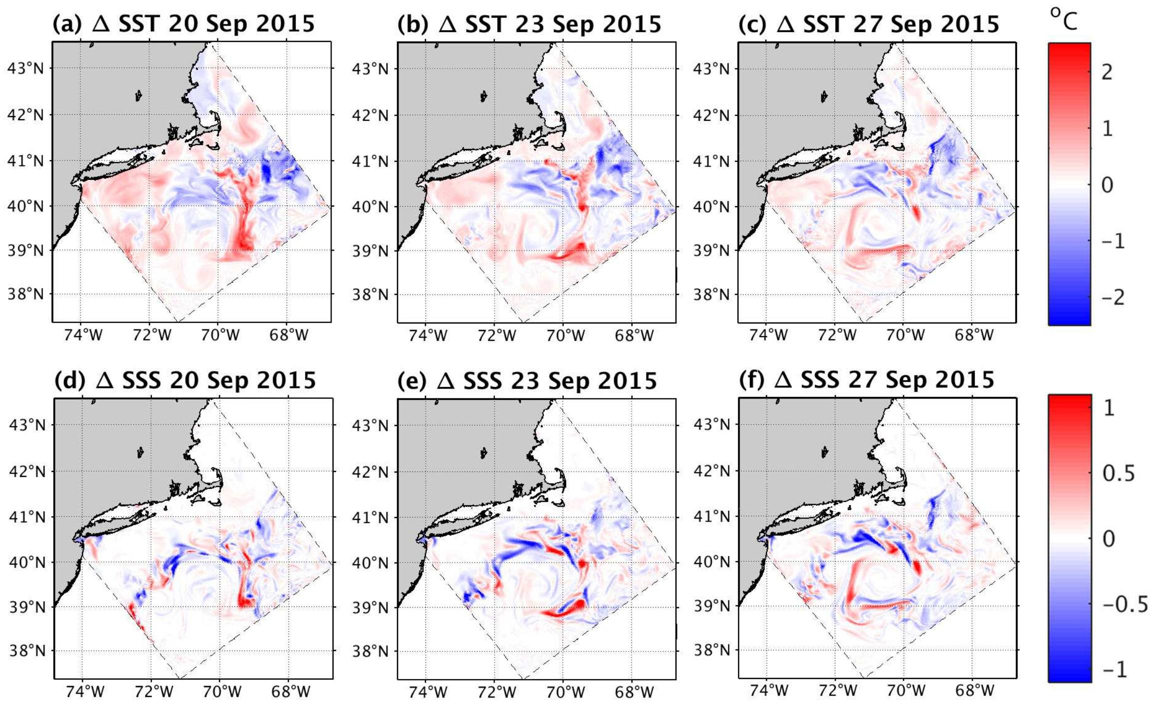

Figure 10: The SST (°C) (a,b,c) and SSS (d,e,f) forecast differences for $\boldsymbol{x}_f^a - \boldsymbol{x}_f^b$ on the days indicated. The 4D-Var analysis increments at the forecast start time are shown in (a) and (d), while (b,e) and (c,f) represent 3-day and 7-day forecast differences, respectively.

Figures 9a-c show an example SST forecast for $\boldsymbol{x}_f^b$ using G2 for the period 20-27 September 2015. The forecast initial condition for SST is shown in Fig. 9a, where a large warm-core Gulf Stream ring dominates the circulation. During the subsequent 7-days of the forecast, the ring circulation evolves, and a filament of cooler, fresher water circulates anticyclonically around the eastern and southern margins of the eddy (Figs. 9b and 9c), while a train of secondary instabilities develops along the ring's northern edge. Figures 9d-o show the square root of the diagonal elements of $\boldsymbol{M}(-\tau,t)\boldsymbol{C}\boldsymbol{M}^T(t,-\tau)$ computed using (7). For brevity, we will refer to these as the "*standard deviations*" but recognize, of course, that the square root of the difference in the background error and analysis error variances *does not* represent the difference between the corresponding standard deviations. The *standard deviations* are shown in Figs. 9d-o for SST, sea surface salinity (SSS), sea surface height (SSH), and surface current speed. Since $\boldsymbol{M}(-\tau,t)\boldsymbol{C}\boldsymbol{M}^T(t,-\tau)$ represents the difference between the background error covariance and the expected analysis error covariance due to assimilating the observations, Figs. 9d-o indicate the *reduction* in the expected analysis and forecast error variance due to assimilating observations during the 4D-Var cycle spanning 17-19 September. The influence of the circulation is very evident in Fig. 9, especially in the case of SST (Figs. 9d,e,f) and SSS (Figs. 9g,h,i). In particular, data assimilation reduces the expected error in the anticyclonic filament of cooler, fresher water by ~1°C (SST) and ~0.5 (SSS). The expected reductions in error *standard deviation* in SSH (Figs. 9j,k,l) and surface current speeds (Figs. 9m,n,o) are more modest and are ~2 cm and ~15 cm s^{-1}, respectively.

The forecast differences $\boldsymbol{x}_f^a - \boldsymbol{x}_f^b$ computed from the nonlinear model forecasts for SST and SSS for the same period are shown in Fig. 10 and are fairly large. For example, Fig. 10 indicates that with the benefit of data assimilation, the forecast initialized from $\boldsymbol{x}^a$ generally leads to an increase in temperature and salinity of the filament that is advected anticyclonically around the eddy. Therefore, the corresponding features in Fig. 9 represent a reduction in the *standard deviation* of the forecast error associated with these changes. Regions in Fig. 9 where the *standard deviations* are close to zero correspond to locations and fields where data assimilation has little impact on the expected forecast error variance and have an error variance similar to the background. This does not mean that the forecast is not accurate, only that the forecast is not benefiting in any significant way from the most recent data assimilated into the model.

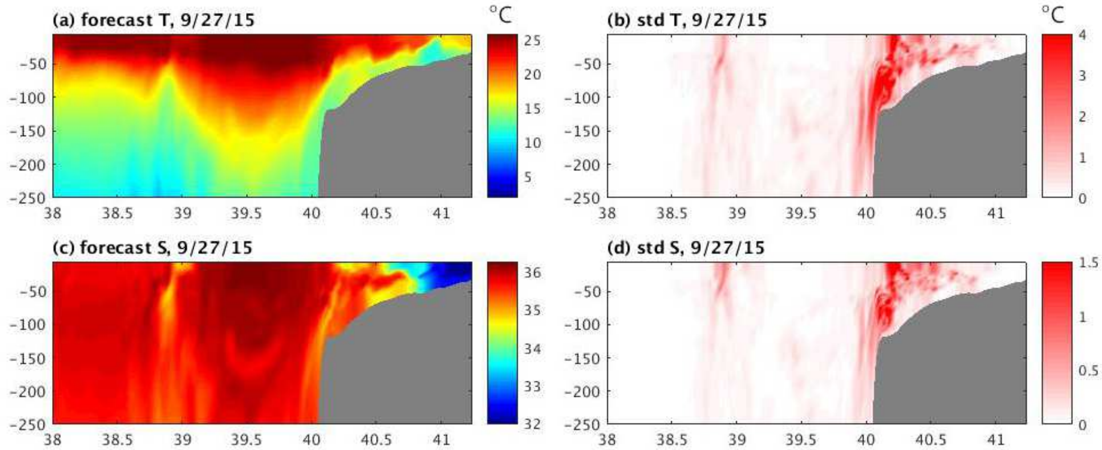

Figure 11: Vertical sections of upper-ocean temperature (ºC) (a) and salinity (c) along 70.5°W on forecast day 7 (27 Sept 2015) for the case shown in Fig. 9. Vertical sections of the *standard deviations* computed from the square-root of the diagonal elements of $\boldsymbol{M}(-\tau,t)\boldsymbol{C}\boldsymbol{M}^T(t,-\tau)$ are also displayed for temperature (ºC) (b) and salinity (d) on the same forecast day.

The vertical structure of the forecast temperature and salinity along 70.5°W over the upper 250 m of the water column is shown in Figs. 11a and 11c, respectively, on forecast day 7. The signature of the warm core ring is very evident, with the main thermocline reaching depths ~150 m in the core of the ring (Fig. 11a). The signature of the cooler, lower salinity filament at the southern edge of the eddy is also visible near 39°N. Figures 11b and 11d show the corresponding vertical structure of the temperature and salinity "*standard deviations*" computed from $\boldsymbol{M}(-\tau,t)\boldsymbol{C}\boldsymbol{M}^T(t,-\tau)$ for the same forecast day. Elevated values of expected error reduction are prevalent on the continental shelf, and following the cooler, lower salinity filament, and extend to depths below 500 m (not shown).

5.2 Spatio-temporal variations

The reduction in *total* expected forecast error variance due to assimilating the observations is $tr\big(\boldsymbol{M}(-\tau,t)\boldsymbol{C}\boldsymbol{M}^T(t,-\tau)\big)$ which can be thought of as the squared distance between $\boldsymbol{x}_f^b(t)$ and $\boldsymbol{x}_f^a(t)$ in Fig. 8. Similarly, the reduction in total variance associated with a particular forecast variable is given by the appropriate sub-trace of $\boldsymbol{M}(-\tau,t)\boldsymbol{C}\boldsymbol{M}^T(t,-\tau)$. The reduction in total variance at forecast time t relative to that the beginning of the forecast cycle provides a measure of the change in the distance between the forecasts $\boldsymbol{x}_f^b(t)$ and $\boldsymbol{x}_f^a(t)$. With this in mind, Fig. 12 shows time series of $\mu(t) = \log_{10}\{tr(\boldsymbol{M}(-\tau,t)\boldsymbol{C}\boldsymbol{M}^T(t,-\tau))/tr(\boldsymbol{M}(-\tau,0)\boldsymbol{C}\boldsymbol{M}^T(0,-\tau))\}$ versus forecast lead-time t (*cf.* Fig. 8) for the sub-trace associated with *all-* temperature grid points. Thus $\mu(t)$ can be viewed as an index of the change in the *relative distance* between the forecasts. Time series are presented for all 2015 forecast cycles on G1 and G2. Instances for which the *relative distance* $\mu(t) > 0$ represent forecast times for which the sub-trace variance at time t is higher than that of the forecast initial condition at time 0 (*cf.* Fig. 8). In other words, the temperature forecasts of $\boldsymbol{x}_f^b(t)$ and $\boldsymbol{x}_f^a(t)$ are farther apart. These situations correspond to cases where the total temperature variance of $\boldsymbol{M}(-\tau,t)\boldsymbol{B}\boldsymbol{M}^T(t,-\tau) - \boldsymbol{M}(-\tau,t)\boldsymbol{A}\boldsymbol{M}^T(t,-\tau)$ increases with forecast lead-time, meaning that the forecasts $\boldsymbol{x}_f^a(t)$ and $\boldsymbol{x}_f^b(t)$ are diverging through time and indicate a persistent benefit of data assimilation for $\boldsymbol{x}_f^a(t)$. Conversely, when the *relative distance* $\mu(t) < 0$, the squared distance between the forecasts $\boldsymbol{x}_f^a(t)$ and $\boldsymbol{x}_f^b(t)$ is decreasing over time, and the benefits of data assimilation for $\boldsymbol{x}_f^a(t)$ are being slowly lost.

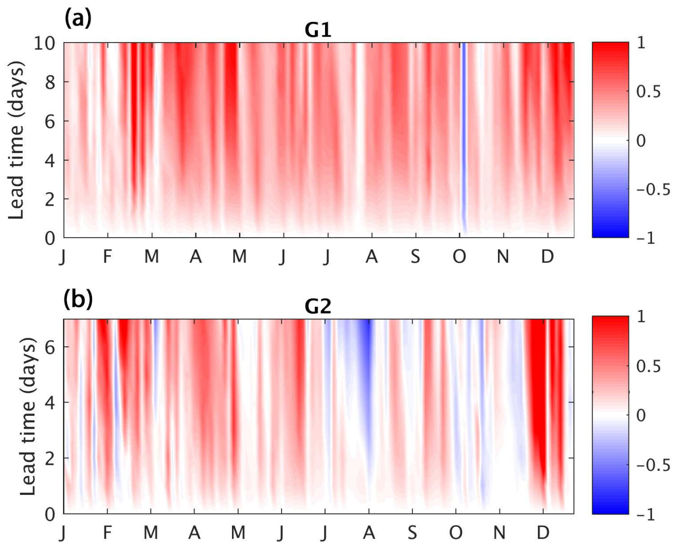

Figure 12: Time series of the *relative distance* between the forecasts $\mu(t) = \log_{10}\{tr(\boldsymbol{M}(-\tau,t)\boldsymbol{C}\boldsymbol{M}^T(t,-\tau))/tr(\boldsymbol{M}(-\tau,0)\boldsymbol{C}\boldsymbol{M}^T(0,-\tau))\}$ for the sub-trace describing the total temperature variance for each 4D-Var analysis-forecast cycle during 2015 in (a) G1 and (b) G2 as a function of forecast lead time.

Figure 12 indicates that for most forecast cycles and lead times, the *relative distance* $\mu(t) > 0$ and the benefits of data assimilation during the 4D-Var analysis cycles extends throughout the forecast interval. This is particularly true for G1 (Fig. 12a). For G2 (Fig. 12b), there are more instances when $\mu(t) < 0$ showing more cases when $\boldsymbol{x}_f^a(t)$ and $\boldsymbol{x}_f^b(t)$ converge in this domain. Time series of $\mu(t)$ for other state-vector fields display similar behavior. Yet, for SSH and velocity, the number of instances when $\mu(t) < 0$ is generally higher than for temperature (not shown). The difference in behavior between G1 and G2 can be understood in terms of the relative horizontal resolution of the two grids. While G2 better resolves the mesoscale instabilities than G1, G2 is more susceptible to the growth of forecast errors due to the more energetic, higher Rossby number, circulation. Being inherently less predictable to the added nonlinearity, we would expect the forecast skill of G2 to degrade on shorter time scales than in G1.

Figures 13a-d show the square root of the mean-variance associated with SST and SSS analyses and 7-day forecasts computed from the average of $\boldsymbol{M}(-\tau,t)\boldsymbol{C}\boldsymbol{M}^T(t,-\tau)$ over *all* analysis-forecast cycles for 2015 in G2. Large reductions in expected error occur in the vicinity of the Pioneer Array and are associated mainly with the observations collected by the array. However, there are significant reductions in the expected error farther afield, clearly related to persistent circulation features, such as the equatorward shelf-break jet in the MAB. The decrease in error can be as large as 3°C in SST and >0.5 in salinity. Also, Figs. 13e-h shows the square root of the mean-variance for analyses and 10-day forecasts in G1. The expected error reduction in the G1 4D-Var analyses and forecasts are quantitatively similar to those in G2 and again highlight the local influence of the Pioneer Array. The larger-scale circulation effect is also evident in G1, with significant reductions in the expected error extending toward Georges Bank because 4D-Var propagates information dynamically upstream to the source region of waters that subsequently flow through the Pioneer Array.

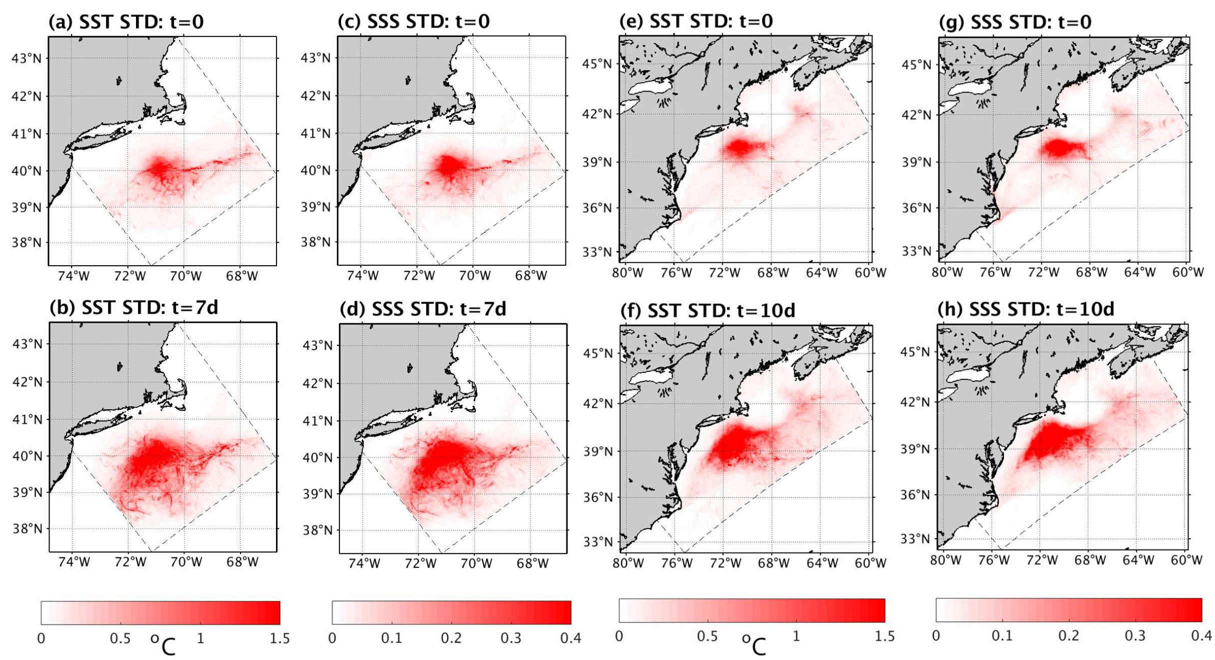

Figure 13: The square root of the average variance for SST (°C) and SSS computed from $\boldsymbol{M}(-\tau,t)\boldsymbol{C}\boldsymbol{M}^T(t,-\tau)$ for all analyses and forecast cycles for G2 (a-d) and G1 (e-h). Forecast day 7 is shown for G2 and forecast day 10 in the case of G1. The color bar is saturated in all instances to accentuate the regions of the highest average variance.

5.3 Observation impacts on analysis and forecast error covariance

Much of the impact of data assimilation on the forecast state given by $\boldsymbol{x}_f^a(t) - \boldsymbol{x}_f^b(t)$ can be attributed to the RAM associated with the smallest eigenvalue. To illustrate, consider again the G2 forecast illustrated in Fig. 10 for the period 20-27 September 2015. Figures 14a and 14b show the SST and SSS components of $\boldsymbol{x}_f^a(t) - \boldsymbol{x}_f^b(t)$ associated with RAM $\widetilde{\boldsymbol{\Psi}}_7$ (*i.e.*, $\tilde{\alpha}_7\boldsymbol{M}(-\tau,t)\widetilde{\boldsymbol{\Psi}}_7$) on forecast day 7 and are very similar to Figs. 10c and 10f. Therefore, much can be learned about the impact of data assimilation on the expected forecast errors from $\widetilde{\boldsymbol{\Psi}}_7$ alone. Furthermore, the good agreement between Figs. 14ab and Figs. 10cf, confirms that the tangent linear approximation remains valid over this timescale.

According to (6), the amplitude of RAM $\widetilde{\boldsymbol{\Psi}}_7$ is given by the dot-product of the innovation vector $\boldsymbol{d}$ with the vector $\tilde{\lambda}_7^{-1}\boldsymbol{R}^{-1}\boldsymbol{H}\boldsymbol{B}\boldsymbol{H}^T\boldsymbol{V}_m\boldsymbol{\varphi}_7$. Therefore, the contribution of each observation to $\tilde{\alpha}_7$ can be quantified. The forecast differences shown in Figs. 14a and 14b result from assimilating observations during the preceding 4D-Var analysis cycle spanning the period 17-19 Sept. Figure 14c shows the contribution of each observation type assimilated during this period to the RAM amplitude $\tilde{\alpha}_7$. The largest contribution is from satellite SST, although *in situ* velocity measurements from the Pioneer Array moorings are a close second. The contribution of *in situ* temperature observations, mainly from Pioneer Array moorings and gliders, are also significant. The location of the *in situ* observations during this 4D-Var cycle are indicated in Fig. 6. Thus, the partitioning of the amplitude of the dominant RAM across the different observing platforms is a useful and alternative approach for quantifying the impact of the assimilated observations on the forecast. The standard method for quantifying observation impacts in ROMS follows the adjoint-approach of Langland and Baker (2004) where the impact of each observation on a chosen analysis or forecast metric is computed. While this approach is generally quite efficient, it requires separate calculations for each metric and forecast lead time. The alternative approach that we are advocating here, however, is independent of any metric and forecast lead time.

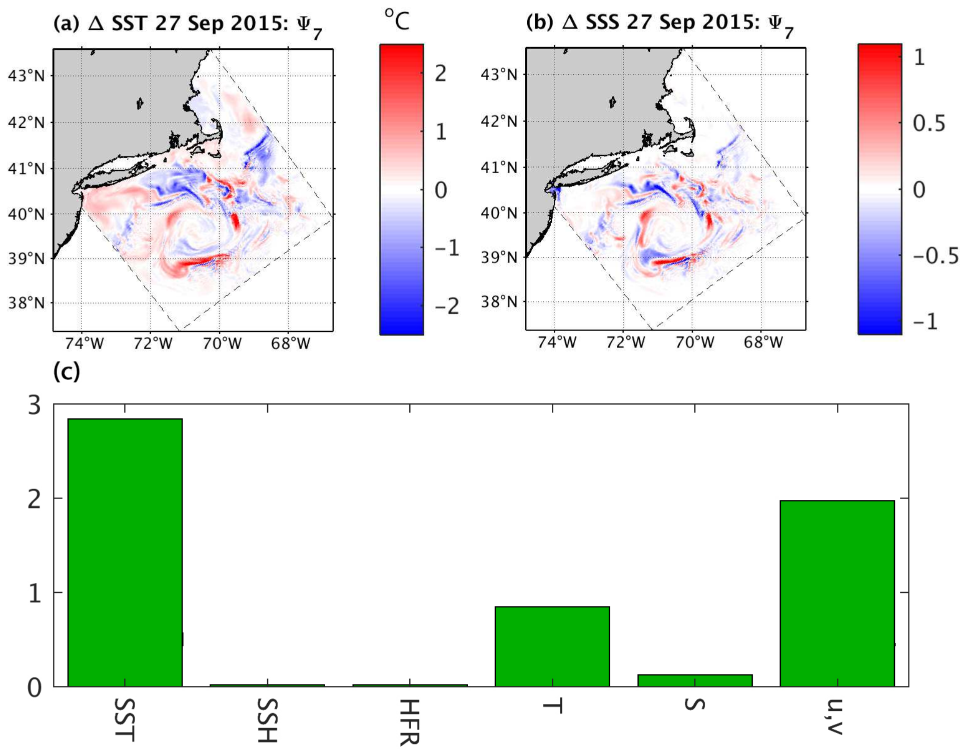

Figure 14: The contribution of $\widetilde{\boldsymbol{\Psi}}_7$ to the G2 SST (ºC) (a) and SSS (b) 7-day forecast differences $\boldsymbol{x}_f^a(t) - \boldsymbol{x}_f^b(t)$ on 27 Sept 2015. (c) The contribution of each observation type assimilated during the pre-forecast 4D-Var cycle (17-19 Sept 2015) to $\tilde{\alpha}_7$: SST – satellite SST; SSH – along-track altimetry; HFR – surface current estimates from coastal HF radar; T,S – *in situ* temperature/salinity observations; u,v – *in situ* velocity observations.

As noted in section 2, the RAMs depend on the observation locations according to (5) and *not* on the observation values. Specifically, $\widetilde{\boldsymbol{\Psi}}_i = \boldsymbol{B}\boldsymbol{H}^T\boldsymbol{V}_m\boldsymbol{\varphi}_i$, where the matrix-vector product $\boldsymbol{V}_m\boldsymbol{\varphi}_i$ represents an EOF of the $\boldsymbol{R}$-preconditioned stabilized representer matrix. In the usual way, these EOFs provide information about the in-phase and out-of-phase relationships between various fractions of the total error variance at different observation locations. Since (5) is a linear equation, each RAM can be expressed as the linear superposition of the contribution from each element of $\boldsymbol{V}_m\boldsymbol{\varphi}_i$ corresponding to specific observations. Figure 15 shows the contribution of the $\boldsymbol{V}_m\boldsymbol{\varphi}_7$ EOF from information associated with the location of satellite SST, *in situ* temperature, and *in situ* velocity observations to the 7-day SST forecast differences of $\boldsymbol{x}_f^a(t) - \boldsymbol{x}_f^b(t)$ for G2 on 27 Sep 2005. In keeping with Fig. 14, the contributions of EOF information at SSH, HFR radar, and *in situ* salinity observation locations are small, so are not shown. Consistent with Fig 14a, the SST component of $\widetilde{\boldsymbol{\Psi}}_7$ in Fig. 15a accounts for much of the forecast change in SST. To the north of the warm core ring and on the continental shelf, the contributions of *in situ* temperature (Fig. 15b) and velocity (Fig. 15c) are mainly in opposition, while around the margins of the ring, these contributions reinforce each other. Thus, while there are considerable, and in some cases opposing, overlaps between the contributions of different observation types to $\widetilde{\boldsymbol{\Psi}}_7$, the general behavior in Fig. 15 confirms the observation impacts computed from the RAM amplitude $\tilde{\alpha}_7$, which depends *directly* on the measurement values.

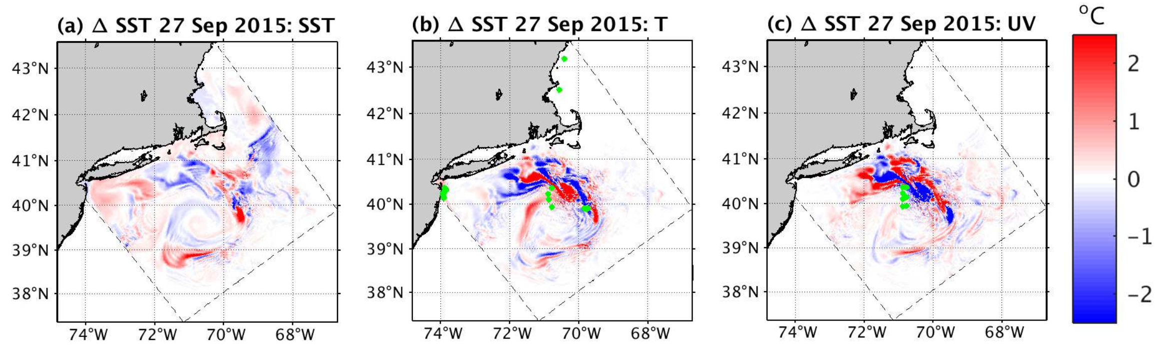

Figure 15: The contribution of the different components of $\boldsymbol{V}_m\boldsymbol{\varphi}_7$ to the G2 7-day SST forecast differences $\boldsymbol{x}_f^a(t) - \boldsymbol{x}_f^b(t)$ on 27 Sept 2015 for: (a) satellite SST, (b) *in situ* temperature observations, (c) *in situ* velocity observations. The locations of the *in situ* observations for temperature and velocity are shown in (b) and (c) as green dots. The units are ºC.

With this in mind, Fig. 16 shows the root mean square (RMS) contribution of each observation type to the RAM $\widetilde{\boldsymbol{\Psi}}_7$ amplitude $\tilde{\alpha}_7$ on each of the three grids. The period considered is Jan 2014 – Dec 2015 which is the overlapping period for which 4D-Var analyses were computed for all three grids. Figure 16 indicates that for a given observation type, this measure of the *observation impact* varies considerably across the three grids. These grid-to-grid variations are controlled by several factors that include: (i) variations associated with differences in data coverage; for example, the number of along-track satellite altimeter overpasses decreases dramatically going from G1 to G2, with very few tracks passing over G3, (ii) variations in horizontal resolution; for example, the increase in the impact of *in situ* velocity observations going from G1 to G3 can be attributed to the greater ability of G3 to resolve unbalanced sub-mesoscale circulations and better utilize velocity observations from Pioneer (Levin *et al.* 2021), and (iii) variations in the 4D-Var background error and observation error covariance matrices $\boldsymbol{B}$ and $\boldsymbol{R}$. The *a priori* assumptions encapsulated in $\boldsymbol{B}$ and $\boldsymbol{R}$ vary from grid-to-grid. As discussed in Levin *et al.* (2020), the parameters used to compute the observation error covariance matrix, $\boldsymbol{R}$, and background error covariance matrix, $\boldsymbol{B}$, are not the same on the three grids. The observation error standard deviations, σ_o, assumed for *in situ* temperature observations are similar across all three grids and range from ~0.6°C on G1 to ~0.4°C on G2 and G3. Yet, *a posteriori* analysis of the innovation statistics following the diagnostics described by Desroziers et al. (2005) suggests that σ_o should be closer to ~1°C, as noted in Levin *et al.* (2020). The *a priori* values of σ_o for *in situ* salinity observations were assumed to ~0.2 on G1, while the *a posteriori* innovation statistics indicate that ~0.4 is a more appropriate choice, the value subsequently adopted for both G2 and G3. This is one reason why the impact of salinity observations declines from G1 to G3. For velocity measurements, σ_o on G1 was assumed to be ~0.6 ms^{-1} for HF radar surface current estimates and ~0.3 ms^{-1} for moorings but were adjusted downwards to ~0.1 ms^{-1} and ~0.04 ms^{-1} respectively on G2 and G3 to be more in line with the *a posteriori* innovation statistics.

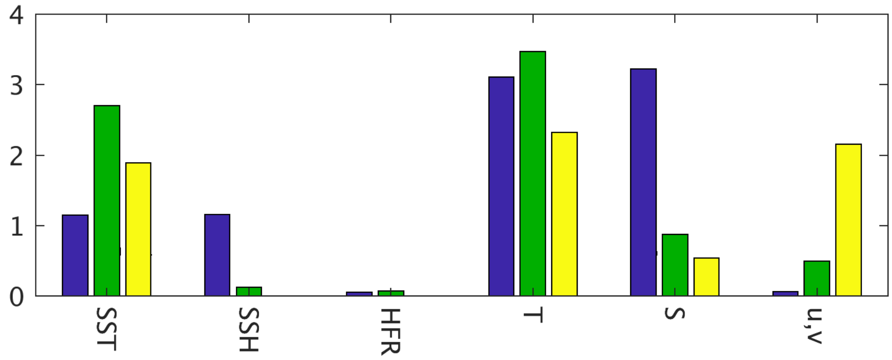

Figure 16: The root mean square contribution of each observation type to $\tilde{\alpha}_7$ averaged over all 4D-Var cycles spanning 2014-2015 for each of the three grids: G1 – blue; G2 – green; G3 – yellow.

The observation impacts in Fig. 16 are generally consistent with the metric-based observation impact calculations presented by Levin *et al.* (2019, 2020, 2021) for the same ROMS configuration computed using the aforementioned adjoint-approach of Langland and Baker (2014). More discussion about the influence of the factors mentioned above on the metric-based observation impacts can be found in Levin *et al.* (2020, 2021).

6 Degrees of Freedom

Consider the situation where N error-free observations are to be assimilated into an ocean model describing an M-dimensional state-space where $N < M$. In principle these observations can provide at most N independent pieces of information about the rank of the tangent linear observation operator $\boldsymbol{H}$ (Rodgers, 2000). However, in the presence of measurement errors (and rounding errors in the estimation problem, that contribute to ill-conditioning), the number of independent pieces of information will be less than N, thus reducing the effective rank of $\boldsymbol{H}$. Eigen analysis of the $\boldsymbol{R}$-preconditioned stabilized representer matrix $\widetilde{\boldsymbol{P}} = (\boldsymbol{R}^{-1}\boldsymbol{H}\boldsymbol{B}\boldsymbol{H}^T + \boldsymbol{I})$ can be used to quantify the effective rank of $\boldsymbol{H}$ by identifying the number of eigenvalues λ greater than 2. The corresponding array modes identify the sub-space that is effectively informed by the observations. Formally, this identifies the *range* of $\boldsymbol{H}$ and, to coin a phrase from Lanczos (1961), represents the part of state-space that is *activated* by the observations. The sub-space orthogonal to the range is referred to as the *null* space. As discussed by Bennett (2002), the number of *df* of the 4D-Var *cost function* is N, and is partitioned between the *df* of the signal and the *df* of the noise due to the presence of observation error. The eigenvectors of $\widetilde{\boldsymbol{P}}$ with eigenvalues $\lambda \gg 2$ contribute most to the *df* of the signal, while eigenvectors of $\widetilde{\boldsymbol{P}}$ with $\lambda < 2$ contribute most to the *df* of the noise.

As shown in section 5, the RAMs associated with the smallest EOF variances λ exert the greatest control on the 4D-Var analyses and ensuing forecasts. It is, therefore, important to determine whether the smaller scale circulation features associated with these RAMs (*e.g.*, Fig. 4g) are reliable and physically relevant, or whether they contribute primarily to noise in the estimate. As noted above, the RAMs can be interpreted as state-space vectors that are associated with the *df* of either the signal or the noise that is resolved by the observing system. Formally, if $\lambda < 2$, the associated RAMs cannot be distinguished from observation error. However, Bennett and McIntosh (1984) have argued for a much more conservative criterion in which fewer array modes are admitted to the analysis by rejecting those $\boldsymbol{\Psi}$ for which $\lambda_i/\lambda_1 < 0.01$. Given the practical difficulties and uncertainties in prescribing $\boldsymbol{B}$ and $\boldsymbol{R}$ for large and complex models, such a strategy seems very prudent. As demonstrated by MAE, the Bennett and McIntosh "1% rule" can be used to gauge the extent to which 4D-Var analyses may suffer from over-fitting to errors in the observations.

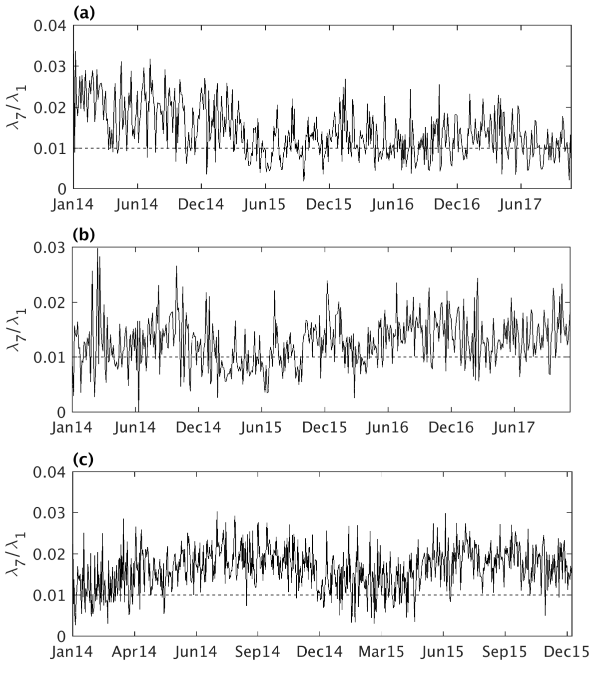

Figure 17: Time series of $\tilde{\lambda}_7/\tilde{\lambda}_1$ for the 1st outer-loop for all 4D-Var cycles on (a) G1, (b) G2, and (c) G3. The black dashed line indicates where $\tilde{\lambda}_7/\tilde{\lambda}_1 = 1$, and represents the cut-off threshold based on the Bennett and McIntosh (1984) "1% rule."

Following MAE, Fig. 17 shows the time series of $\tilde{\lambda}_7/\tilde{\lambda}_1$ during the 1st outer-loop for the 4D-Var analyses on the three grids. During the majority of cycles, $\tilde{\lambda}_7/\tilde{\lambda}_1 > 0.01$ on all three grids although there are a significant number of cycles for which $\tilde{\lambda}_7/\tilde{\lambda}_1 < 0.01$, particularly on G1 and G2, suggesting that we may be dangerously close to over-fitting the model to observation errors during these cycles. In these cases, the observations that control most RAM $\widetilde{\mathbf{\Psi}}_7$ may, in fact, be exerting an overly large impact on the analyses and forecasts. The situation is better on G3, where $\tilde{\lambda}_7/\tilde{\lambda}_1$ exhibits a seasonal cycle with a tendency for potential over-fitting during winter months. While this aspect of the data assimilation system clearly warrants further attention, Fig. 17 highlights how the RAMs can identify and monitor endemic issues within the system.

7 Summary and Conclusions

In this paper, we have explored the properties of the MAB and GoM ocean observing systems using the RAMs of a state-of-the-art 4D-Var data assimilation system in a triply nested configuration of ROMS. Central to this work are two complementary interpretations of the RAMs. First, they provide information about the *df* of the observing system (in light of *a priori* assumptions about the background error covariance), and the 3-dimensional structures of the RAMs (*cf*. Fig. 6) provide a clear representation of the *field-of-view* of the observing array. This property of the RAMs has been exploited here to quantify the extent to which data assimilation reduces errors in ocean analyses and forecasts. Second, the RAMs can be interpreted as interpolation patterns for the observations into state-space (Bennett, 1985). We capitalize on this exegesis of the RAMs to elucidate the efficacy of the resulting ocean state estimates.

In the present case, Fig. 7 indicates that the RAMs associated with the *most* stable interpolation patterns on all three grids appear to be most strongly controlled by the *in situ* observations from the Pioneer Array. It is these observations that will generally contribute most significantly to the *df* of the signal. Given that the *in situ* observing platforms are in principle relocatable, an interesting future study would be to explore the extent to which the MAB and GoM observing system could be reconfigured and "optimized" to potentially provide a more complete view of the upper ocean circulation. Array modes have recently been used in this way by Le Hénaff *et al.* (2009) and Lamouroux *et al.* (2016) to evaluate different observing system designs in the Bay of Biscay. Remote sensing observations are an essential component of the observing system, and in contrast to *in situ* observations, Fig. 7 suggests that they appear to control the 3-dimensional structures of the *least* stable RAMs. Thus, uncertainties in remote sensing data are likely to be the largest contributors to uncertainties in the ocean state estimates, and potentially contribute most to the *df* of the noise. However, the observation impact calculations discussed below suggest that this is not always the case.

A novel application of the RAMs presented here quantifies the extent to which ocean forecasts benefit from data assimilation. This was achieved by time-evolving the RAMs from each analysis cycle through the forecast interval, and using the known covariance properties of the RAM amplitudes to compute the difference between the expected forecast error covariances of forecasts with and without data assimilation, namely $\boldsymbol{MBM}^T - \boldsymbol{MAM}^T$. This type of analysis reveals first-hand how intimately the expected covariance properties of the forecast errors are tied to the underlying circulation. In addition, they quantify the extent to which information gained from data assimilation persists throughout the forecast. Our analyses also reveal the extent to which the observations can inform the forecast both locally and remotely through the circulation dynamics, which in this study spans a variety of complex circulation regimes ranging from quasi-geostrophic down to the sub-mesoscale. The Pioneer Array provides a powerful example of this last point in the present study. This is graphically illustrated in Fig. 13, which indicates the extent to which information from the Pioneer Array, in concert with the other elements of the observing system, is conveyed to other parts of the model domain. This study represents a proof-of-concept of the methodology and was applied to cases where forecasts were initialized from 4D-Var analysis computed using a single outer-loop. More work is required to adapt the method to the case of multiple outer-loops.

Since the RAM-based approach for quantifying the expected reduction in error covariance is predicated on the tangent linear approximation, it is natural to enquire to what extent this approximation remains valid over the ~10-day duration of the combined analysis-forecast cycles employed here. If $\Delta\boldsymbol{x}(t)$ denotes the state-vector difference between the nonlinear model forecasts $\boldsymbol{x}_f^a(t)$ and $\boldsymbol{x}_f^b(t)$, and $\delta\boldsymbol{x}(t)$ is the corresponding forecast difference based on the RAMs, then the correlation between $\Delta\boldsymbol{x}(t)$ and $\delta\boldsymbol{x}(t)$ versus lead time t provides a quantitative measure of the efficacy of the tangent linear approximation. Such an analysis on G1 and G2 (not shown) reveals a pronounced seasonal cycle with the lowest correlations during winter, and peak correlations during the summer. During winter, the cooling of the shelf waters enhances the horizontal temperature gradients in the vicinity of the Gulf Stream temperature front. This, in turn, will presumably favor faster growth of $\delta\boldsymbol{x}$ (and $\Delta\boldsymbol{x}$) via baroclinic instabilities and is most likely a major reason why the tangent linear assumption is less robust during wintertime. However, much of the wintertime drop in correlation can be attributed to short length-scales associated with differences in localized perturbation growth of $\Delta\boldsymbol{x}(t)$ and $\delta\boldsymbol{x}(t)$. If both are spatially low pass filtered, the average correlations between them are much improved at longer forecast lead-times and, for surface fields at a 7-day lead-time, correlations are typically greater than 0.5. Therefore, we feel confident that the patterns of error covariance, such as Figs. 9 and 11, provide useful information about the regions where forecasts are informed by data assimilation for periods ~1 week.

An alternative approach for quantifying the impact of the observations on the expected analysis and forecast error covariance has also been explored here. The procedure is based on the contribution of each observation to the amplitude of the *least* stable RAM, in our case $\widetilde{\boldsymbol{\Psi}}_7$. What this of course suggests is that RAMs that may contribute most significantly to the *df* of the noise, are in fact the most impactful on the analyses and forecasts. The second equality in (6) shows that the RAM amplitudes can be expressed as $\tilde{\alpha}_7 = \tilde{\lambda}_7^{-1}\boldsymbol{d}^T\boldsymbol{R}^{-1}\boldsymbol{H}\widetilde{\boldsymbol{\Psi}}_7$. Thus, there are two important factors that control the contribution (aka impact) of different observations on $\tilde{\alpha}_7$ for the least stable RAM. First, the RAM is sampled in observation space (*i.e.* $\boldsymbol{H}\widetilde{\boldsymbol{\Psi}}_7$). Therefore, it is reasonable to assume that the observations that will exert the most influence on the RAM structure will also have a large impact on $\tilde{\alpha}$ since $\boldsymbol{H}\widetilde{\boldsymbol{\Psi}}_7$ represents a resampling of the RAM at the locations of those very same observations. Second, the resampled RAM is rescaled by the inverse observation error variances ($\boldsymbol{R}^{-1}$), which will assign greater weight to observations with small expected errors. As discussed in section 5.2, these factors weigh-in to differing degrees in the results of Fig. 16 which shows the RMS contribution of different observations to the dot-product of the innovation vector $\boldsymbol{d}$ with the vector $\tilde{\lambda}_7^{-1}\boldsymbol{R}^{-1}\boldsymbol{H}\widetilde{\boldsymbol{\Psi}}_7$. Figure 16 indicates that *in situ* observations are generally as impactful as SST observations. Therefore, while it is tempting from

Figs. 7b,d,f to attribute much of the structure of the least stable RAM to remote sensing observations, Fig. 16 indicates that *in situ* observations contribute significantly also.

The most common approach used at operational centers to quantify observation impacts on analyses and forecasts is metric-based, and as such, the observation impacts can vary across different metrics and through time. Conversely, the alternative approach introduced here is metric-independent, and quantifies the impact of the observations during *any* phase of the analysis and forecast cycle (while the tangent linear assumption remains valid) since the RAM amplitudes, for a given assimilation cycle, are time-invariant. The utility of the RAM-based approach will be evaluated in some of the near real-time systems currently being run in support of U.S. IOOS and reported later.

Another practical application of the RAMs applied here is monitoring of the efficacy of the 4D-Var ocean state estimates. Specifically, an *a posteriori* analysis of the eigenvalues of the preconditioned stabilized representer matrix associated with 4D-Var analyses across the three nested grids suggests that the current system configuration may be uncomfortably close to overfitting the model to errors in the observations. This overfitting could potentially introduce unphysical features into the analyses, and it seems likely, based on Fig. 7, that the primary culprit is satellite observations. Therefore, some adjustments of the near real-time analysis-forecast system are probably warranted. Even though we have employed the lenient "1% rule" of Bennett and McIntosh (1984), the issue of overfitting deserves further attention and should be a cautionary tale for others engaged in ocean data assimilation who may also find that they too are unknowingly flirting with the detrimental influences of observation error.

The RAMs are straightforward to compute using the archived output from the 4D-Var system, and we have shown here that they can be a useful tool for monitoring the performance of a data assimilation system, and for placing bounds on the expected errors of ensuing forecasts. However, it is also of interest to speculate on additional important practical applications that capitalize on the properties of the RAMs. Specifically, since the RAMs provide flow-dependent covariance information (*i.e.*, they are derived from the EOFs of the total expected rescaled error variance), they also have considerable potential utility for improving the data assimilation system itself. In particular, it has been demonstrated in numerical weather prediction (*e.g.*, Lorenc *et al.*, 2015) that hybrid data assimilation approaches that combine climatological covariance information about the background errors with flow-dependent information about "errors of the day" generally out-perform systems that use this information independently. Hybrid approaches are also an active area of research in oceanography (see Moore *et al*. 2019). The ROMS 4D-Var system falls into the first category in that the background error covariance matrix $\boldsymbol{B}$ is based on climatological information. However, one can imagine a hybrid approach in which $\boldsymbol{B} = \gamma_c \boldsymbol{B}_c + \gamma_a \boldsymbol{B}_a$ where $\boldsymbol{B}_c$ is the standard climatological background error covariance, and $\boldsymbol{B}_a$ is a flow-dependent background error covariance based on the RAMs, and that varies from cycle-to-cycle. The coefficients γ_c and γ_a are weights that can be determined based on theoretical considerations (Ménétrier and Auligné, 2015). For example, if we let $\boldsymbol{B}_a = \boldsymbol{C}$ and choose $\gamma_c = 1$ and $\gamma_a = -1$, then we will recover a reduced-rank approximation of $\boldsymbol{A}$, although what we really require for data assimilation is $\boldsymbol{MAM}^T$, as discussed in section 5.1. Ensemble methods are commonly used to estimate flow-dependent covariance information. However, due to the necessarily limited size of the ensemble, some form of localization is generally required to eliminate spurious correlations, which can be a computationally expensive procedure (Houtekamer and Zhang, 2016). One advantage of using the RAMs to construct $\boldsymbol{B}_a$ is that the expected covariance properties of the RAM amplitudes is known *a priori* (*cf*. equation (7)) which circumvents the obvious need for localization since $\boldsymbol{C}$ in (7) represents the expected covariance arising from an *infinite* ensemble. To illustrate the flow-dependent information captured by $\boldsymbol{C}$, Fig. 18 shows the *standard deviations* of SSS derived from $\boldsymbol{C}$ for the 4D-Var analyses shown in Fig. 1 on 16 May 2014. The richness of the field and variance information is very evident and becomes increasingly more complex as the grid resolution increases. It would be next to impossible to adequately model the inhomogeneous fields, like those in Fig. 18, using conventional approaches to $\boldsymbol{B}_c$, such as diffusion operators (as in section 3). Therefore, the RAMs offer a straightforward and convenient procedure for supplementing $\boldsymbol{B}$. Information about the cross-covariances between the different components of the state-vector, and associated correlation length scales, is naturally embedded in $\boldsymbol{C}$ from which a hybrid approach can benefit. Even though $\boldsymbol{B}_c$ is only weakly flow-dependent, 4D-Var is forgiving since $\boldsymbol{HBH}^T$ in (2) provides implicit flow-dependent covariance information. It is this information that is mined by the RAMs and mapped to state-space by $\boldsymbol{BH}^T$ and which we argue we can capitalize on using the approach that we are advocating here for constructing $\boldsymbol{B}_a$.

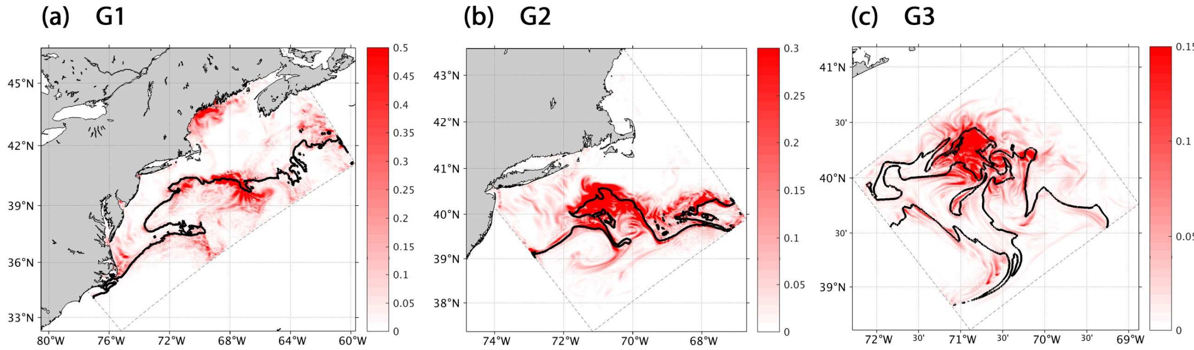

Figure 18: The square root of the reduction in expected analysis error variance in SSS for the same 4D-Var analysis shown in Fig. 1 for 16 May 2014. The 34.5 isohaline is also shown in each panel (black line) as a proxy for the Mid-Atlantic Bight shelf-break front position.

With steady progress in the resolution capabilities of satellite altimeters and radiometers, and the advent of new, innovative, mobile, and adaptive observing platforms such as gliders and other autonomous underwater vehicles (AUVs), data assimilation at the ocean sub-mesoscale is a new and exciting frontier. Dense *in situ* observing systems, such as the Pioneer Array, offer extraordinary and unprecedented insight into the sub-mesoscale environment. Synthesizing these data using ocean models and data assimilation, however, represents a considerable challenge. From this perspective, Fig. 18c is particularly exciting since it reveals the remarkable level of detail that can potentially be mined to develop an effective hybrid 4D-Var approach for ROMS. The sub-mesoscale forecast problem on G3 has not been considered here but is, nonetheless important, and will be the subject of a future study.

Acknowledgments

This work was supported by grants from the National Science Foundation (OCE-1459665 and OCE-1459646), NASA (NNX17AH58G) and NOAA (NA16NOS0120020). Pioneer Array data were obtained from the NSF Ocean Observatories Initiative Data Portal http://ooinet.oceanobservatories.org.

References

Andersson, E., Järvinen, H., 1999. Variational quality control. *Q. J. R. Meteorol. Soc*. **125**, 679-722.

Bennett, A. F. ,1985. Array design by inverse methods. *Progress in Oceanography*, **15**, 129–156.

Bennett, A. F., 2002. Inverse modeling of the ocean and atmosphere (234 pp.). Cambridge, UK: Cambridge University Press.

Bennett, A. F., McIntosh, P. C., 1984. Open ocean modelling as an inverse problem: M2 tides in Bass Strait. *Journal of Physical Oceanography,* **14**, 601–614.

Boyer, T., Antonov, J., Baranova, O., Garcia, H., Johnson, D., Locarnini, R., Mishonov, A., OBrien, T., Seidov, D., Smolyar, I., Zweng, M., 2009. World ocean database 2009. In: Levitus, S. (Ed.), NOAA Atlas NESDIS 66, 216pp.

Chen, Y., Wang, C.-F., 2015. Characteristic modes: Theory and applications in antenna engineering (269 pp.). Hoboken, NJ: John Wiley and Sons.

Courtier, P., Thépaut, J.N., Hollingsworth, A., 1994. A strategy for operational implemenation of 4D-Var using an incremental approach. *Quart. J. R. Meteorol. Soc*. **120**, 1367-1388.

Daley, R., 1991. Atmospheric Data Analysis. Cambridge University Press, 457pp.

Desroziers, G., Berre, L., Chapnik, B., Poli, P., 2005. Diagnosis of observation, background and analysis-error statistics in observation space. *Q. J. R. Meteorol. Soc*. **131**, 3385-3396.

Egbert, G.D., Bennett, A.F., Foreman, M.G.G., 1994. TOPEX/POSEISON tides estimated using a global inverse model. *J. Geophys. Res.*, **99**, 24,821-24,852.

Fairall, C., Bradley, E., Hare, J., Grachev, A., Ebson, J., Young, G., 2003. Bulk parameterization of airsea fluxes: updates and verification for the COARE algorithm. *J. Climate* **16**, 571–591.

Fisher, M., Courtier, P., 1995. Estimating the covariance matrices of analysis and forecast error in variational data assimilation. *ECMWF Tech. Memo*., **220**, 28.

Fleming, N., 2016. Seasonal and spatial variability in temperature, salinity and circulation of the Middle Atlantic Bight. PhD thesis, 336pp.

Gawarkiewicz, G., Todd, R., Zhang, W., Partida, J., Gangopadhyay, A., Monim, M.U.H., Fratantoni, P., Malik, A.M., Dent, M., 2018. The changing nature of shelf-break exchange revealed by the OOI Pioneer Array. *Oceanography* **31**, 60–90.

Gratton, S., Tshimanga, J., 2009. An observation-space formulation of variational assimilation using a restricted preconditioned conjugate gradient algorithm. *Q. J. R. Meteorol. Soc*., **135**, 1573-1585.

Gürol, S., Weaver, A., Moore, A., Piacentini, A., Arango, H., Gratton, S., 2014. B-preconditioned minimization algorithms for variational data assimilation with the dual formulation. *Quart. J. R. Meteorol. Soc.* **140**, 539–556.

Houtekamer, P.L. and Zhang, F., 2016. Review of the ensemble Kalman filter for atmospheric data assimilation. *Mon. Weather Rev.*, **144**, 4489-4531.

Kurapov, A. L., G. D. Egbert, J. S. Allen, Miller, R.N., 2009. Representer-based analyses in the coastal upwelling system. *Dynamics of Atmospheres and Oceans*, **48**, 198-218.

Kurapov, A. L., Özkan-Haller, H.T., 2013. Bathymetry correction using an adjoint component of a coupled nearshore wave-circulation model: Tests with synthetic velocity data, *J. Geophys. Res. Oceans*., **118**, 4673-4688.

Lamouroux, J., Charria, G., De Mey, P., Raynaud, S., Hayraud, C., Craneguy, P., Dumas, F. and Le Hénaff, M., 2016: Objective assessment of the contribution of the RECOPESCA network to the monitoring of 3D coastal ocean variables in the Bay of Biscay and the English Channel. *Ocean Dynamics*, **66**, 567-588.

Lanczos, C., 1961. Linear Differential Operators. D. Van Nostrand Company Ltd, London and New York, 564pp.

Langland, R., Baker, N., 2004. Estimation of observation impact using the NRL atmospheric variational data assimilation adjoint system. *Tellus* **56A**, 109–201.

Le Hénaff, M., De Mey, P., Marsaleix, P., 2009. Assessment of observational networks with the representer matrix spectra method-application to a 3D coastal model of the Bay of Biscay. *Ocean Dyn*. **59**, 3–20.

Lellouche, J.-M., Greiner, E., Le Galloudec, O., Garric, G., Regnier, C., Drevillon, M., Benkiran, M., Testut, C.-E., Bourdalle-Badie, R., Gasparin, F., Hernandez, O., Levier, B., Drillet, Y., Remy, E., and Le Traon, P.-Y., 2018. Recent updates to the Copernicus Marine Service global ocean monitoring and forecasting real-time 1/12° high-resolution system, Ocean Sci., 14, 1093–1126, doi: 10.5194/os-14-1093-2018.

Levin, J., Wilkin, J., Fleming, N., Zavala-Garay, J., 2018. Mean circulation of the mid-Atlantic Bight from a climatological data assimilative model. *Ocean Model*. **128**, 1–14.

Levin, J., Arango, H.G., Laughlin, B., Wilkin, J., Moore, A.M., 2019. The impact of remote sensing observations on cross-shelf transport estimates from 4D-Var analyses of the Mid-Atlantic Bight. *Advances in Space Research*, https://doi.org/10.1016/j.asr.2019.09.012

Levin, J., Arango, H.G., Laughlin, B., Hunter, E., Wilkin, J., Moore, A.M., 2020. Observation Impacts on the Mid-Atlantic Bight Front and Cross-Shelf Transport in 4D-Var Ocean State Estimates: Part I – Multiplatform analysis, *Ocean Modelling*, **156**, https://doi.org/10.1016/j.ocemod.2020.101721.

Levin, J., Arango, H.G., Laughlin, B., Hunter, E., Wilkin, J., Moore, A.M., 2021. Observation Impacts on the Mid-Atlantic Bight Front and Cross-Shelf Transport in 4D-Var Ocean State Estimates: Part II – The Pioneer Array, *Ocean Modelling*, **157**, https://doi.org/10.1016/j.ocemod.2020.101731.

Liu, J. and Kalnay, E., 2008: Estimating observation impact without adjoint model in an ensemble Kalman filter. *Q. J. R. Meteorol. Soc.*, **134**, 1327–1335.

Lopez, A. G., Wilkin, J.L., Levin, J.C., 2020. Doppio – A ROMS-based Circulation Model for the Mid-Atlantic Bight and Gulf of Maine: Configuration and comparison to integrated coastal observing network observations, Geosci. Model Dev. Discuss., https://doi.org/10.5194/gmd-2019-359, submitted.

Lorenc, A.C., Bowler, N., Clayton, A.M., Pringa, S.R., Fairbairn, D., 2015: Comparison of Hybrid-4DEnVar and Hybrid-4DVar Data Assimilation Methods for Global NWP. *Mon. Weather Rev.*, **143**, 212-229.

Ménétrier, B., Auligné, T., 2015: Optimized Localization and Hybridization to Filter Ensemble-Based Covariances. *Mon. Weather Rev.*, **143**, 3931-3947.

Moore, A.M., Arango, P., 2021. On the behavior of ocean analysis and forecast error covariance in the presence of baroclinic instability. *Ocean Modelling*, **157**, https://doi.org/10.1016/j.ocemod.2020.101733.

Moore, A.M., Arango, H.G., Broquet, G., Edwards, C.A., Veneziani, M., Foley, B.P.D., Doyle, J., Costa, D., Robinson, P., 2011a. The Regional Ocean Modeling System (ROMS) 4-dimensional variational data assimilation systems. Part I: System overview and formulation. *Prog. Oceanogr*. **91**, 34–49.

Moore, A.M., Arango, H.G., Broquet, G., Edwards, C.A., Veneziani, M., Foley, B.P.D., Doyle, J., Costa, D., Robinson, P., 2011b. The Regional Ocean Modeling System (ROMS) 4-dimensional variational data assimilation systems. Part II: Performance and application to the California Current System. *Prog. Oceanogr*. **91**, 50–73.

Moore, A.M., Arango, H.G., Edwards, C.A., 2018: Reduced-rank array modes of the California Current observing system. *J. Geophys. Res.*, **122**, doi:10.1002/2017JC013172

Moore, A.M., Martin, M.J., Akella, S., Arango, H.G., Balmaseda, M., Bertino, L., Ciavatta, S., Cornuelle, B., Cummings, J., Frolov, S., Lermusiaux, P., Oddo, P., Oke, P.R., Sorto, A., Teruzzi, A., Vidard, A., Weaver, A.T., 2019. Synthesis of Ocean Observations using Data Assimilation for Operational, Real-time and Reanalysis Systems: A More Complete Picture of the State of the Ocean. *Frontiers in Marine Science* **6:90**. doi:10.3389/fmars.2019.00090.

Ngodock, H., Souopgui, I., Carrier, M., Smith, S., Osborne, J., D'Addezio, J., 2020. An ensemble of perturbed analyses to approximate the analysis error covariance in 4dvar, *Tellus* A: *Dynamic Meteorology and Oceanography*, **72:1**, 1-12, DOI:10.1080/16000870.2020.1771069

Rodgers, C.D., 2000: Inverse Methods for Atmospheres: Theory and Practice. *Series on Atmospheric, Oceanic and Planetary Physics, World Scientific Publ., Singapore*, 238pp.

Weaver, A., Courtier, P., 2001. Correlation modelling on the sphere using a generalized diffusion equation. *Quart. J. R. Meteorol. Soc.* **127**, 1815–1846.

Wilkin, J., Levin, J., Lopez, A., Hunter, E., Zavala-Garay, J., Arango, H., 2018. A Coastal Ocean Forecast System for U.S. Mid-Atlantic Bight and Gulf of Maine. In: Chassignet, E.P., Pascual, A., TintoreÅL, J., Verron, J. (Eds.), New Frontiers in Operational Oceanography, pp. 593–624 (Chapter 21).

Zhang, W., Gawarkiewicz, G., 2015. Dynamics of the direct intrusion of Gulf Stream ring water onto the Mid-Atlantic Bight shelf. *Geophys. Res. Lett*. **42**. https://doi.org/10.1002/2015GL065530.